Methods to determine the radiated power in SPI-mitigated disruptions in JET

J. Lovell,[1, a)] M. L. Reinke,[1] U. A. Sheikh,[2] R. Sweeney,[3] P. Puglia,[2] P. Carvalho,[4] L. Baylor,[1] and JET Contributors[b)]

[1)] *Oak Ridge National Laboratory, Oak Ridge, TN 37831, USA*

[2)] *École Polytechnique Fédérale de Lausanne (EPFL), Swiss Plasma Center (SPC), CH-1015 Lausanne, Switzerland*

[3)] *MIT Plasma Science and Fusion Center, Cambridge, MA 01239, USA*

[4)] *Instituto de Plasmas e Fusão Nuclear, Instituto Superior Técnico, Lisbon 1049-001, Portugal*

This paper presents techniques for evaluating the radiated power in JET disruptions. Disrupting plasmas are shown to have non-axisymmetric radiation profiles, motivating re-evaluation of the standard techniques for calculating the total radiated power at JET using bolometry. Four single-channel bolometers at different toroidal locations are exploited to quantify the radiation asymmetry. Toroidal radiation peaking factors integrated over the entire disruption of up to 1.5 have been observed when varying the quantity of neon in pellets used in disruptions mitigated by shattered pellet injection (SPI). Using synthetic bolometer diagnostics developed with the Cherab spectroscopy modelling framework we can estimate the systematic error on total power calculations for relevant radiation profiles and improve estimates of the total radiated power. We show that the component of the systematic error on the total power due to the poloidal radiation profile can be reduced from 70% to 10% with suitable assumptions about the structure of the poloidal profile.

[a)] jack.lovell@ukaea.uk

[b)] See the author list of E. Joffrin et al. accepted for publication in Nuclear Fusion Special issue 2019, https://doi.org/10.1088/1741-4326/ab2276

I. INTRODUCTION

Disruptions in large tokamaks represent a significant risk to the device[1]. Sudden loss of plasma confinement can lead to large forces acting on the vessel, and extremely high heat loads on plasma-facing components (PFCs). In order to protect its PFCs, ITER requires 95% of the pre-disruption thermal energy in the plasma to be radiated by a disruption mitigation system (DMS)[2].

The shattered pellet injector (SPI) has been chosen for use in the ITER DMS, and an SPI system has recently been installed on the JET tokamak[3]. In order to quantify the effectiveness of the SPI system it is necessary to have accurate measurements of the power radiated during the disruption. However, JET's radiated power diagnostics were not optimised for measuring disruption radiation, which is both extremely short lived and highly asymmetric, particularly in the thermal quench[4]. This is because the bolometer diagnostic consists of two toroidally-spaced, poloidally-viewing systems which cannot be combined without *a priori* knowledge about the toroidal distribution of radiation. As such, the methods for calculating the total radiated power in routine JET plasmas have significant systematic errors which need to be understood and quantified in order to interpret measurements from new SPI experiments. These experiments use the SPI to induce disruptions in otherwise healthy plasmas, but the analysis presented here is just as valid for these cases as it is for cases where the SPI is used to mitigate disruptive plasmas.

We present in this paper analysis of two major sources of systematic error in the calculation of radiated power in JET disruptions. The limited toroidal coverage of radiation diagnostics in JET requires us to make assumptions about the toroidal distribution of radiation. A lack of toroidal symmetry will introduce a systematic error to the calculation of total radiated power. Section II illustrates the use of four toroidal single-channel bolometers to demonstrate the presence of such radiation asymmetries in SPI-mitigated disruptions in JET. Section III describes the estimation of an additional systematic error when the total radiated power is calculated using a weighted sum of individual bolometer brightness measurements, a method which is required for toroidally-asymmetric radiation profiles. Section IV presents the overall conclusions of the work.

II. MEASUREMENTS OF TOROIDAL RADIATION ASYMMETRY

The key diagnostic for calculating the total radiated power in JET is the KB5 bolometer system[5]. This consists of two arrays of gold foil bolometers, one in Octant 3 viewing vertically downwards from the top of the machine (KB5V), and one in Octant 6 viewing horizontally from the outboard to the inboard side (KB5H). These bolometer arrays are displaced toroidally from the SPI, which is installed on top of the vessel in Octant 1. During disruption experiments the bolometers can achieve time resolutions of 1 ms. The lines of sight of the bolometers are shown in Figure 1. To calculate the total power, a tomographic inversion of the brightness measurements of both arrays may be performed, and the resulting poloidal emissivity profile extrapolated around the machine and summed. This method requires a toroidally-symmetric radiation profile in order to relate the measurements in the two different octants. This is not necessarily the case during disruptions. An alternative method uses a weighted sum of the brightness measurements in just one of the arrays, making it possible to use either KB5V or KB5H alone when the radiation profile is non-axisymmetric. This method will be discussed in more detail in Section III, but for now it is important to note that, like the tomographic inversion, it calculates the total radiation in a single poloidal plane and then assumes axisymmetry to estimate the total power from this plane.

We cannot assume that the power measured during the disruption in a single poloidal plane can be extrapolated uniformly around the torus. Previous work on disruptions using massive gas injection (MGI) at Alcator C-Mod[6,7], DIII-D[4] and JET[8] has shown that the radiation during the thermal quench is not toroidally symmetric. We need information about the magnitude and distribution of any toroidal asymmetry: is the radiation toroidally peaked, is it spreading on flux tubes fed by the SPI fragments, or does it have a low-n toroidal variation due to MHD? Are we measuring near a peak of the radiation (in which case, assuming axisymmetry would over-estimate the total radiated power), or near a minimum in a periodic toroidal radiation profile (in which case we would under-estimate the total radiation)? With only one or two toroidal measurements it is not possible to answer these questions definitively.

JET does have another bolometer system, KB1, which provides 4 channels with identical poloidal fields of view at 4 different octants: 2, 3, 6 and 7. The toroidal positions and poloidal field of view of these channels relative to the KB5 arrays are also shown in Figure 1.

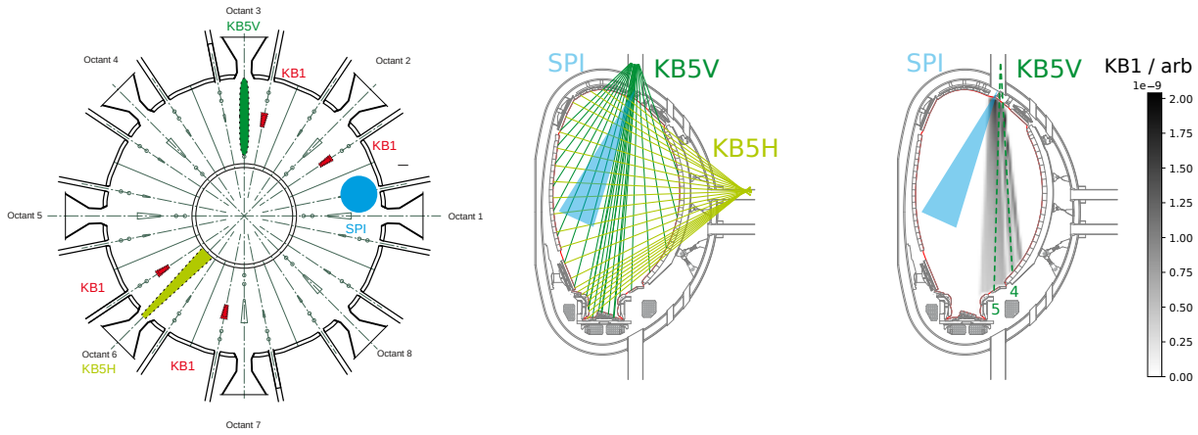

FIG. 1: Left: toroidal positions of the 4 single bolometers of the JET KB1 diagnostic, along with the vertical (KB5V) and horizontal (KB5H) arrays of the KB5 diagnostic. Also shown is the location of the SPI. Centre: the lines of sight of the vertical and horizontal bolometers in the poloidal plane, along with the approximate distribution of the SPI plume. Right: the field of view of the KB1 diagnostic, where the shading indicates the volumetric sensitivity of the detector as a function of position calculated using the Cherab framework, also with the SPI plume. Two KB5V channels, 4 and 5, share a similar poloidal field of view to KB1.

These channels view the low field side (LFS) of the plasma, outside of the divertor. The two narrow regions of reduced sensitivity in the KB1 field of view, near the LFS edge of the FOV and in a similar poloidal region as channel 4 of KB5V, are due to partial obstructions of the view by discrete field coils which share the same port. This bolometer system is not as suited to fast measurements as KB5: typically 100 ms time resolution is achievable with acceptable signal quality.

With these KB1 channels, we have an additional 4 data points to use to estimate the degree of radiation asymmetry. It is important to note that the KB1 system is unable to distinguish between toroidal asymmetries where only the magnitude of the poloidal emissivity profile varies toroidally, and asymmetries where the poloidal profile itself is also varying toroidally and is out of the field of view of the sensors in some octants. Nevertheless, KB1 is still a valuable tool for evaluating the degree of asymmetry to illustrate the limits of interpreting the KB5 data.

In addition to the restricted field of view, there are further challenges in the interpretation

of the KB1 bolometer data. These 4 single-channel bolometers are the last remaining hardware from the original JET bolometer system installed in 1985[9]. Unlike the KB5 bolometers, the detectors use a half-bridge construction, with two resistors located in the electronics and two in the sensor. This, combined with long lengths of cabling and imperfect grounding, makes these channels susceptible to noise. To calculate the radiated power P (in Watts) a 0D heat balance equation is used which requires the time derivative of the measured voltage signal V and two calibration coefficients: the foil's sensitivity S (V/W) and cooling time τ (s)[10].

$$P = \frac{1}{S}\left(V + \tau\frac{\mathrm{d}V}{\mathrm{d}t}\right) \tag{1}$$

Taking the time derivative further amplifies the noise on the signal. The noise ends up being so high that these bolometers are typically not able to provide useful measurements of radiated power in most JET discharges. However, during a disruption the bolometer voltage signal is up to a factor of 10 larger than during a steady state plasma, so the signal-to-noise ratio increases and the data becomes useful.

Equation 1 requires that there is no DC offset in the measured voltage: $P = 0$ implies $V = 0$ for $t \gg \tau$. In reality, the resistors in the bridge circuit are not perfectly balanced and there may be some pickup within the cables, so there is some residual voltage "offset". This offset voltage is measured both before the plasma breakdown and many cooling times after the plasma ends, when we expect $V = 0$. The offset voltage may vary throughout the pulse; to correct for this we take the offset at any point in time during the pulse to be a linear interpolation between the start and end measurements of the voltage. Higher order variations in the offset will be an additional source of noise, but we expect them to be small relative to a DC offset, any linear drift in this offset, and random pickup noise during the pulse.

Another issue to be overcome is that, unlike the KB5 bolometers, the KB1 bolometers have no in-situ calibration capability. Thus the sensitivity S and cooling time τ in equation 1 need to be determined from plasma measurements. The cooling time is typically obtained by fitting an exponential decay to the voltage signal immediately after a disruption, where equation 1 can be solved for $P = 0$. For the voltage V to remain measurable, the power P must drop on a time scale much shorter than the time constant of the foil, which is typically of order 100 ms. In JET it takes several seconds to ramp down the plasma current and thus

the radiation, so a disruption is required to provide a suitably fast step down in P.

Immediately post-disruption the neutral pressure in the region of the bolometer sensors is typically high — the theoretical maximum pressure rise in the vessel from the largest (12 mm diameter) SPI pellet is 50 mBar — and this can reduce the cooling time of the bolometer compared with the vacuum value which is appropriate for the thermal quench. Previous work[11] has shown that the cooling time for typical gold foil bolometers reduces compared with its value in vacuum at pressures as low as 0.1 mBar, so even if the bolometers experience a pressure rise of only a few percent of this theoretical maximum the effect on the cooling time will be noticeable. The cooling time is therefore varying in the several seconds after the disruption; fitting the cooling curve to a single value of τ will introduce some additional systematic error. This effect could be corrected by fitting to multiple windows throughout the cooling period, but noise in the raw data limits how short these windows can be and so will not be able to completely eliminate this source of error.

The sensitivity has been previously calculated by cross-calibration with the poloidal tomography system (KB5). Tomographic reconstructions using KB5 have been integrated along the field of view of the KB1 bolometers to calculate the expected power and the ratio of expected and measured powers gives an estimate of the sensitivity. The shortcoming of this approach is that there are relatively few suitable tomographic reconstructions available — typically < 10 per pulse for the $< 10\%$ of JET pulses with KB1 operational which have reconstructions — and those that are available only apply to very short time windows. The method is therefore very sensitive to noise in the KB1 measurements, and as such there is a large uncertainty on the sensitivity. This leads to large systematic errors of approximately 60% when using KB1 to measure toroidal peaking during disruptions.

A more robust method to calculate the relative sensitivity, used to evaluate the toroidally-varying component of the radiation measured by the 4 channels, is presented here. In non-disruptive JET discharges we expect good toroidal symmetry, and therefore the total radiated energy Q measured by each of the KB1 bolometers should be the same. We use the measured energy to the sensor rather than the power because it avoids the need to calculate the time derivative:

$$\begin{aligned} Q(T) &= \int_0^T \frac{1}{S}\left(V + \tau\frac{\mathrm{d}V}{\mathrm{d}t}\right)\mathrm{d}t \\ &= \frac{1}{S}\int_0^T V\mathrm{d}t + \frac{\tau}{S}\left(V(t=T) - V(t=0)\right) \end{aligned} \tag{2}$$

By choosing T to be at the end of the acquisition window, $V(t=T) = V(t=0) = 0$ and the second term disappears. Since $Q(T)$ must be equal for all channels, the sensitivity S of one channel relative to another S_{ref} is then given by:

$$\frac{S}{S_{ref}} = \frac{\int_0^\infty V\mathrm{d}t}{\int_0^\infty V_{ref}\mathrm{d}t} \tag{3}$$

This method has a number of advantages. It is independent of the cooling time of the channels, so uncertainties in the cooling time calculation do not propagate to the sensitivity value. It avoids the time derivative, so is less sensitive to randomly-varying noise: integrating over the entire pulse makes it even less sensitive to noise than the raw voltage measurement. Finally, it can be performed for any JET discharge with a radiating plasma which did not disrupt, of which there are many more than there are suitable tomographic reconstructions. In this work we selected discharges over 3 years of JET operations between 2016 and 2019, when the KB1 system was installed and working reliably, which had bulk radiated energies calculated using non-divertor-viewing KB5 channels of >16 MJ. This provided hundreds of discharges with large enough radiated energy that the signal to noise ratio of the KB1 energies was good, and enabled us to provide uncertainties on the relative sensitivities. Figure 2 shows a subset of this data from early in the JET C38 campaign, between July and August 2019, illustrating the extent of the scatter in the calculated relative sensitivities due to the high noise levels on individual channels.

With these relative calibrations between the 4 bolometers we begin to characterise the toroidal asymmetries. Figure 3 shows $Q(T)$, calculated using equation 2, over the course of two JET pulses which terminated in SPI-mitigated disruptions. The sensitivity values S were normalised such that the measured energy $Q(T)$ averaged over $t > 15$ s and octants 3, 6 and 7 was equal to 1.0 for each pulse. Pulse 96048 used a pure neon SPI pellet with 4.5 mm diameter and the plasma had a stored energy $W_P = 4.6$ MJ. Pulse 96187 used a larger pure neon pellet, of 8 mm diameter, and the plasma had a stored energy of 5.1 MJ. In both pulses it is clear that there is good toroidal symmetry from 0 s when breakdown occurs, through the Ohmic phase to 9 s and also through the H-mode phase from 9 s to 11 s. There is then

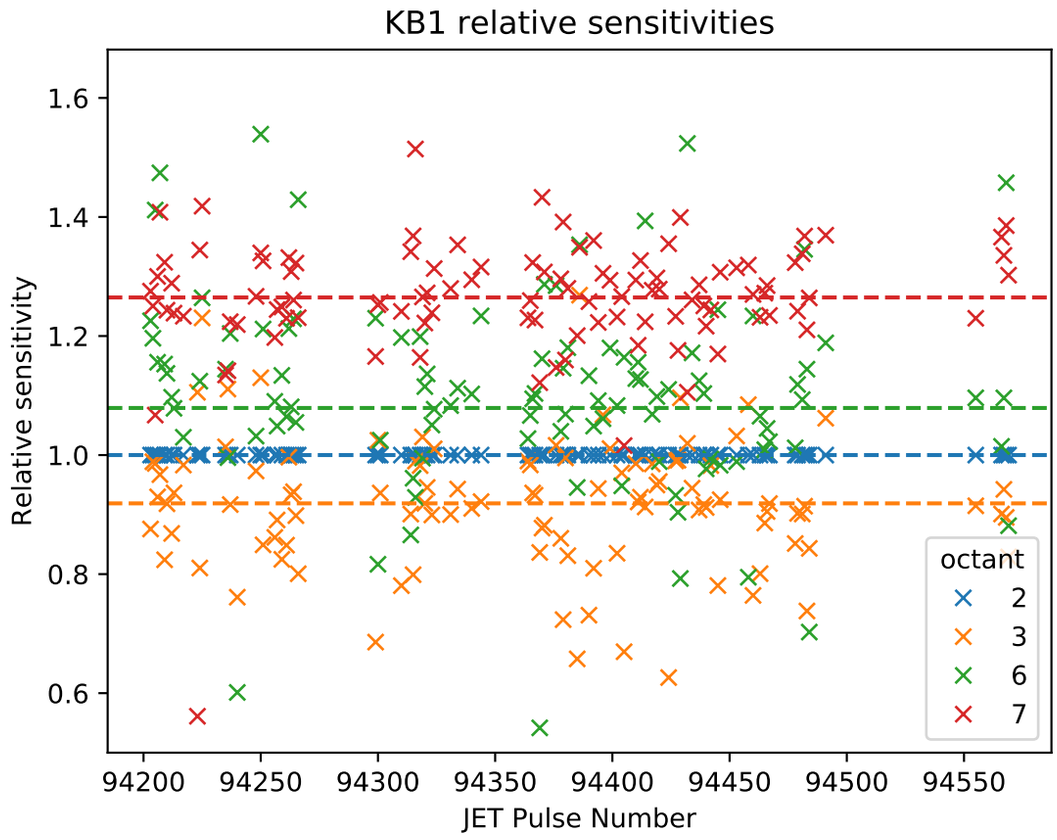

FIG. 2: Calculated KB1 sensitivities relative to the sensitivity of the Octant 2 detector, over a subset of JET pulses. The dotted line represents the mean relative sensitivity of each channel.

a sudden increase in the total radiated energy due to the disruption. There is some time variation within each channel of the total radiated energy even after the disruption: this is due to the cooling time varying with changing neutral pressure in the vessel immediately after the disruption as described above, but this effect becomes negligible after a couple of seconds.

The increase in the radiated energy during the disruption is similar for all 4 channels in 96048, whereas in 96187 (with a larger pellet and higher stored energy) there is a significant asymmetry. The Octant 2 bolometer — which is closest to the SPI injection in Octant 1 — measures significantly higher radiated energy than the Octant 3, 6, and 7 channels, showing peaking near the SPI injection as might be expected. Note also that the channels

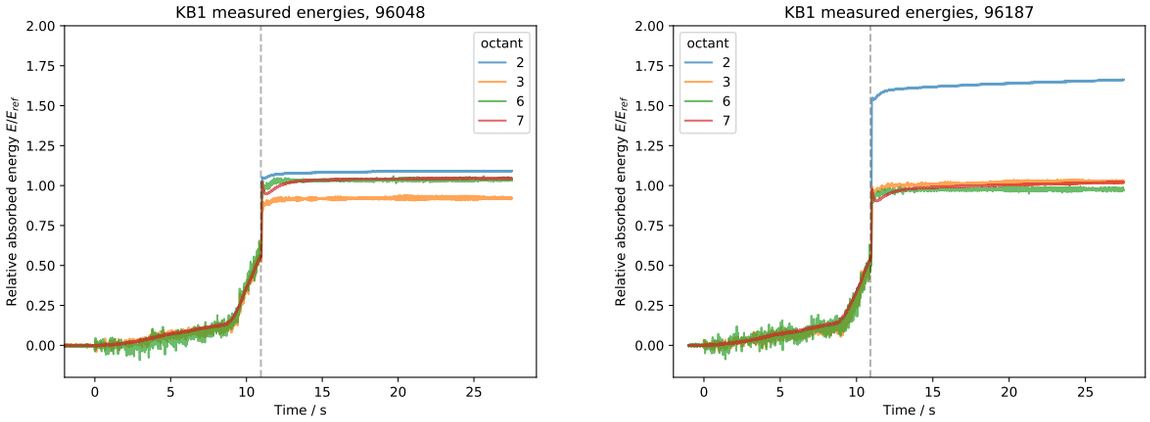

FIG. 3: Time histories of relative radiated energy absorbed by each of the 4 KB1 bolometers in two JET pulses which terminated in SPI-mitigated disruptions at approximately 11 s (dotted line). The reference value E_{ref} is defined as the average value of the post-disruption ($t > 15$ s) cumulative energy measured by the detectors in octants 3, 6 and 7. There is clearly a stronger toroidal asymmetry in the disruption in pulse 96187, which had higher stored energy and a larger pellet, compared with 96048.

in Octants 3 and 6, where the vertical and horizontal KB5 bolometers used to estimate the total radiated power are located, measure significantly less radiation than the octant 2 bolometer. These results suggest that changes to the calculated radiated fraction using the KB5 bolometers, in experiments where pellet size, pellet composition and plasma thermal energy are varied, may be in part due to changes to the toroidal asymmetry of the radiation. A smaller fraction of the total radiation in the poloidal plane of one of the KB5 bolometer arrays due to variations in the toroidal asymmetry, even if the total radiation is in fact not varying, could be incorrectly interpreted as a reduction in the total radiated power.

We define a radiation peaking factor for the disruption to be:

$$f_{peak} = \frac{\max(\Delta Q_i)}{\mathrm{mean}(\Delta Q_i)} \tag{4}$$

ΔQ_i is the difference between the pre- and post-disruption radiated energy for each bolometer. $f_{peak} = 1$ corresponds to full toroidal symmetry.

With this definition, S_{ref} in equation 3 cancels out in the calculation of f_{peak}. We take the post-disruption radiated energy at $T \to \infty$, because the slow integration time of the KB1 electronics (100 ms) and the strong dependence on the poorly-calibrated cooling time τ

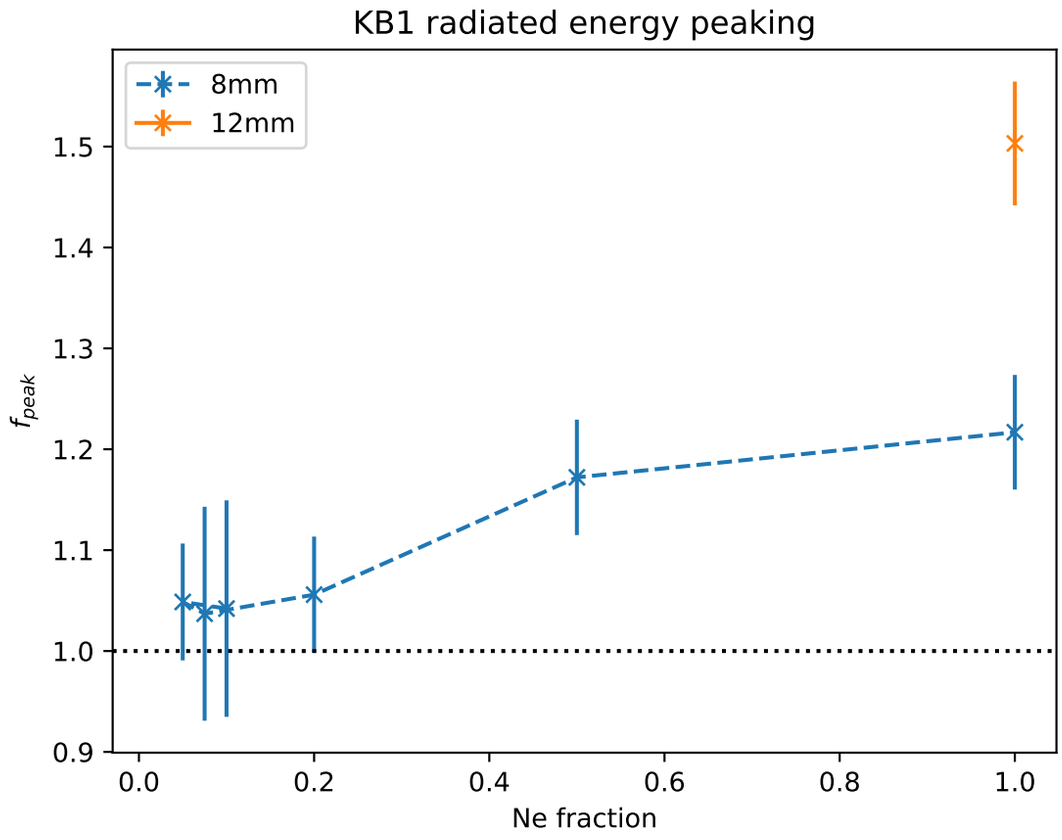

FIG. 4: Radiation peaking f_{peak} vs neon particle fraction in SPI-induced disruptions using neon pellets. The legend shows the pellet diameter. Radiation peaking increases with increasing neon particle fraction, where the neon particle fraction is defined as the ratio of the number of Ne atoms in the pellet to the number of neon atoms in a pure Ne pellet of the same size.

in equation 2 make it difficult to accurately measure radiation just from the thermal quench with these bolometers. Assuming the current quench is toroidally symmetric (as suggested by fast camera data), this analysis will therefore provide a lower bound on the radiation peaking in the thermal quench. Further analysis to obtain the peaking value in the thermal quench itself is left to future work.

This measure of radiation peaking over the entire disruption (thermal quench and current quench) does still provide useful insights. Figure 4 shows the variation in radiation peaking f for disruptions mitigated with the SPI using pellets containing a mixture of deuterium and

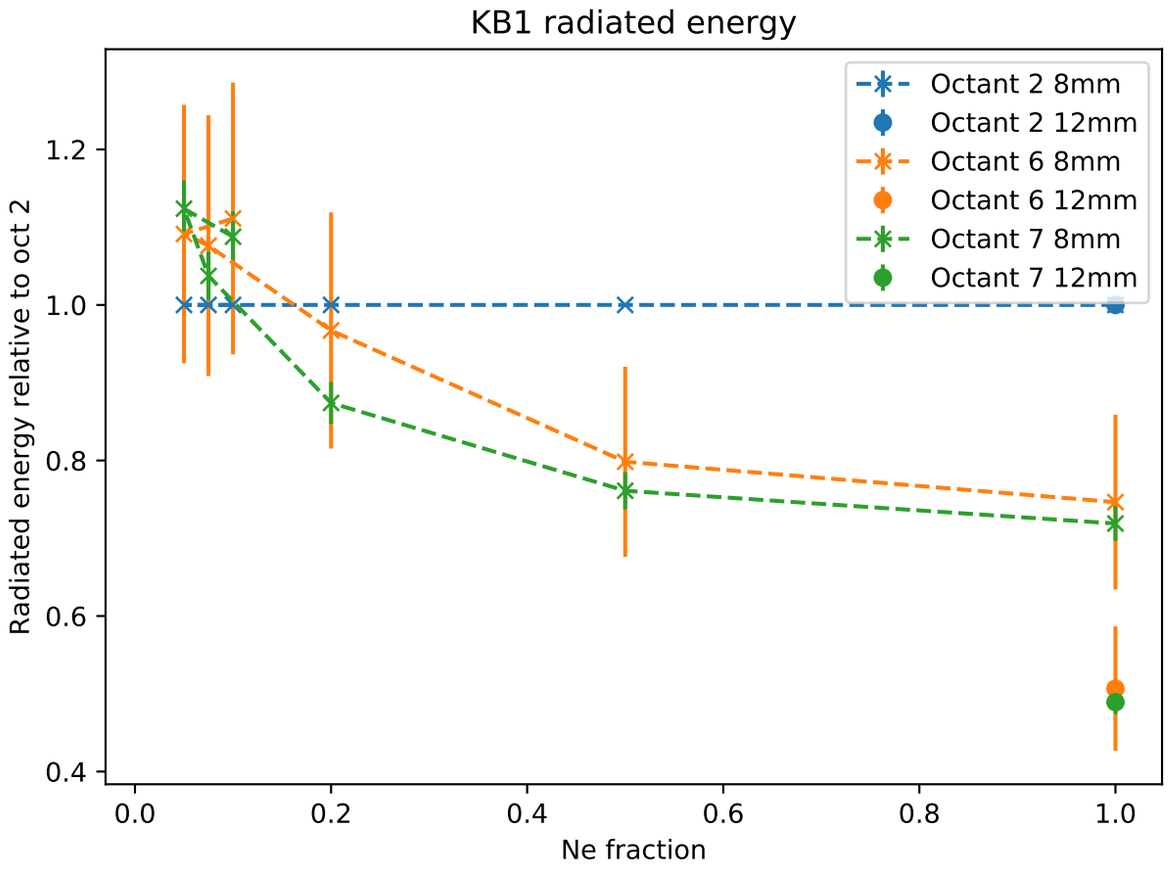

FIG. 5: Radiated energies, relative to the energy measured by the Octant 2 bolometer, vs neon particle fraction. At higher neon fractions the Octant 2 bolometer consistently measures the highest radiated energy.

neon, as the amount of neon in the pellet is varied. All these disruptions occurred in similar $B_t = 2.5\,\mathrm{T}$, $I_p = 2.5\,\mathrm{MA}$, $W_p = 4\,\mathrm{MJ}$ plasmas. We see that higher levels of neon, either through increased neon concentration in pellets of the same size or by moving to a larger pellet size, correlate with an increased peaking over the entire disruption. Figure 5 shows that whenever peaking is present it is consistently the Octant 2 bolometer which measures the highest radiation. This needs to be taken into account when using the radiated power measured by the horizontal KB5 bolometer, in Octant 6, to estimate the total radiated power: simply extrapolating the KB5 Octant 6 measurement is likely to under-estimate the total radiated power.

III. TOTAL RADIATED POWER UNCERTAINTY QUANTIFICATION

The two arrays of the KB5 bolometer system, shown in Figure 1, together provide sufficient coverage of the poloidal cross section to enable tomographic reconstructions of the poloidal radiated power profile from which the total radiated power can be calculated. This method requires the radiation profile to be toroidally symmetric, so that both Octant 3 and Octant 6 systems can be assumed to be measuring the same radiation profile and also so that the total power can be accurately calculated by extrapolating the calculated poloidal emissivity profile around the entire machine. We have however shown in Section II that the radiation in the disruption is not necessarily toroidally symmetric. This makes it impossible to perform a tomographic inversion with JET's bolometer systems as is done for typical, non-disrupting time slices.

Another method exists to estimate the total radiated power: using a weighted sum of the measurements from the channels in one of the two arrays. The weighted sum using the vertical (Octant 3) array is routinely used in JET's inter-shot analysis to estimate the total radiated power, as it is significantly quicker than performing a tomographic inversion and integrating the resulting emissivity profile. The weights are calculated by projecting the lines of sight of the channels into a space where all lines are parallel rather than fanning out, and then applying an additional scaling to the channels viewing the divertor to account for the fact that most radiation from these channels is expected to be in the divertor region. This has been compared with selected tomographic reconstructions and found to be accurate to within about 10% for "standard" JET plasmas (elongated, with a lower X point and a radiating divertor), but this is not the case during the thermal quench. An alternative weighted sum method does not apply the additional scaling for the divertor channels, and is found to better match tomographic inversions in plasmas where main chamber radiation dominates (such as limiter plasmas): we expect this method to better approximate the radiated power in a disruption. Both the scaled and unscaled weighted sum methods are described in detail in reference[12].

The weighted-sum method can be used for the horizontal array too, with the weights calculated in the same way by projecting the lines of sight into a space where they are parallel and calculating the separation between lines of sight. The horizontal array is not routinely used to calculate the total radiated power in standard JET plasmas because none

of its channels view the outer divertor leg where a significant fraction of the radiation is emitted, but as previously stated this is not an issue in disruptions.

Using the weighted sum methods for both the Octant 3 and Octant 6 bolometer systems provides two independent measurements of the total radiated power, without relying on toroidal symmetry. It is important to quantify the uncertainty on these two methods. We have no tomographic inversions to rely on for comparison in disrupting plasmas, so we must instead use a synthetic diagnostic. For this we have turned to the Cherab framework[13], which enables forward modelling of diagnostics based on spectroscopic plasma emission and 3D ray tracing. We load a full 3D CAD model of the JET machine, define a 3D emissivity profile (a "phantom") and trace rays from the bolometer sensors to calculate the total power the bolometers would measure for the given emissivity profile. We then take these bolometer power measurements and calculate the total power using the weighted sum method, for both the vertical and horizontal arrays. The total power is independently calculated by integrating the phantom's emissivity profile over the volume inside the JET first wall. By comparing the weighted sum with this volumetric integral we can estimate the systematic error on the weighted sum method.

The actual 3D emissivity profile of the radiation in the thermal quench is not well known, so we have chosen several different functional forms for the profile. The methods described here can be easily extended to include parameterised models informed by 3D MHD codes such as JOREK[14] or M3D-C1[15] as they become available after further validation of SPI experiments. We define the emissivity at a given toroidal location by a 2D (R, Z) poloidal profile which is then assumed to be toroidally symmetric within a single bolometer array's field of view.

The first poloidal profile used is a simple bivariate Gaussian blob, with a defined centre (R_0, Z_0) and widths δR and δZ defining the standard deviations in the radial and vertical directions respectively. An example is shown in Figure 6. We have also investigated flux-aligned radiation profiles, which are bivariate normal distributions in flux space with a centre defined by the normalised flux surface ψ_0 and poloidal angle θ_0 around the magnetic axis of a JET equilibrium reconstruction taken from the H-mode phase of one of the SPI target plasmas. An example of this is shown in Figure 7. This will not necessarily be an accurate representation of the arrangement of the magnetic field during the disruption, but its purpose is to examine the sensitivity of our study to phantom shape rather than provide an accurate

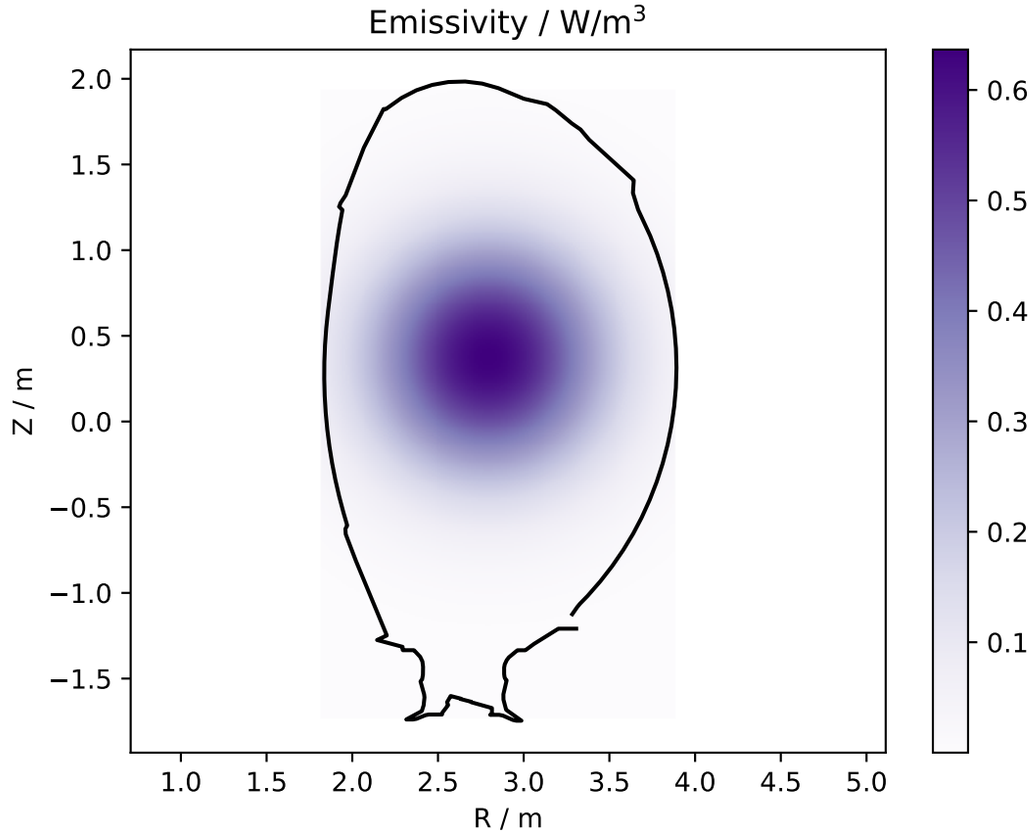

FIG. 6: An example emissivity profile in the R-Z plane, used to evaluate the error on the total radiated power calculated with a weighted sum. This example shows a Gaussian phantom, defined by mean position and standard deviations in R-Z space.

predictive model of the emission. In any case, we expect the bulk of the radiation to be emitted in the thermal quench, and the shape of the LCFS will not change dramatically until the current quench.

Using only a single bolometer array for the weighted sum means we are unable to spatially localise the emission. To evaluate the systematic error, we therefore scan over a range of positions and sizes of phantoms and evaluate both the weighted sum calculation and the total power from the phantom. The results for a selection of Gaussian phantoms, all of width 0.2 m and height 0.5 m but with varying position, are plotted in Figures 8 and 9 for the vertical and horizontal arrays respectively. Note that some of these phantoms have mean positions (R_0, Z_0) which are outside of the JET vessel, but the finite size of these phantoms

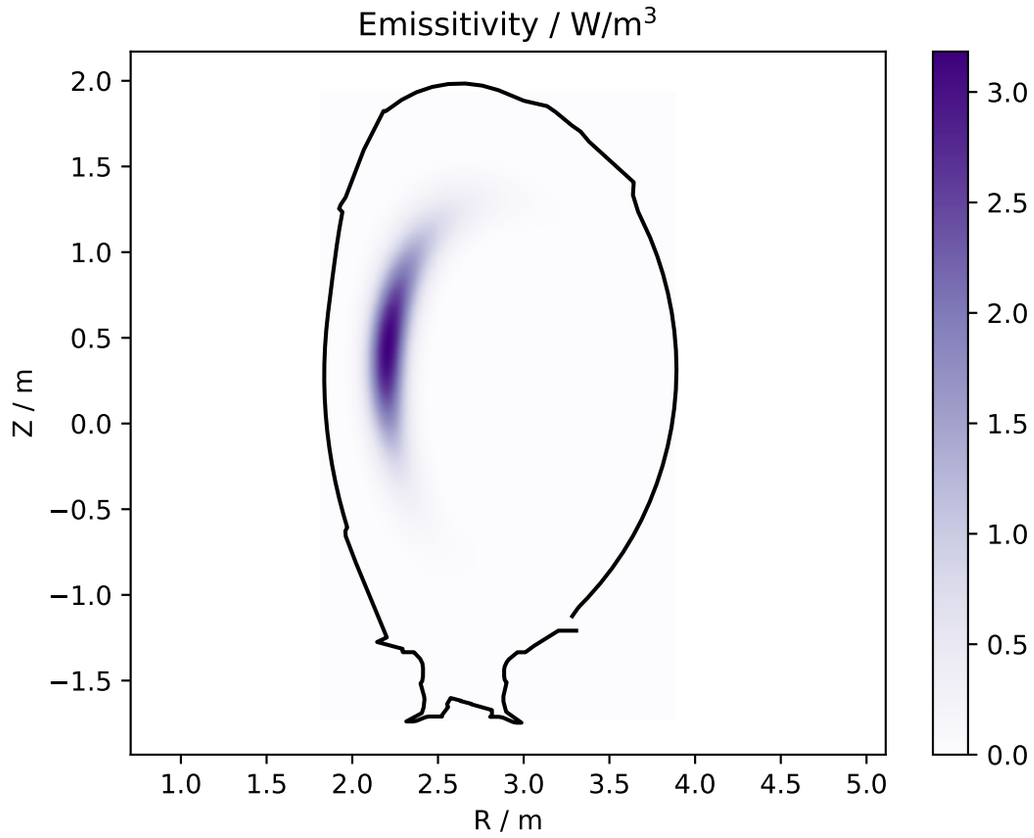

FIG. 7: An example emissivity profile in the R-Z plane, used to evaluate the error on the total radiated power calculated with a weighted sum. This example shows a flux-aligned phantom, defined by a mean and standard deviation flux surface and poloidal angle.

means that they still have a non-zero amount of radiation inside the vessel. Conversely, some of the phantoms with mean positions inside the vessel but close to the wall will have some non-zero emissivity outside of the vessel. As previously discussed, we consider only the radiation inside the vessel when calculating the total power the phantom.

We can see that for the vertical array the use of the weighted sum causes the total power to be underestimated most of the time, except when the radiation is peaked at the top of the device near to the bolometers themselves where the weighted sum significantly overestimates the total power. The strong sensitivity to position is consistent with sections 4.2 and 4.3 in reference[12], which suggest the optimal set of weights to use in the sum is dependent on the poloidal distribution of the radiation profile. The weighted sum using the

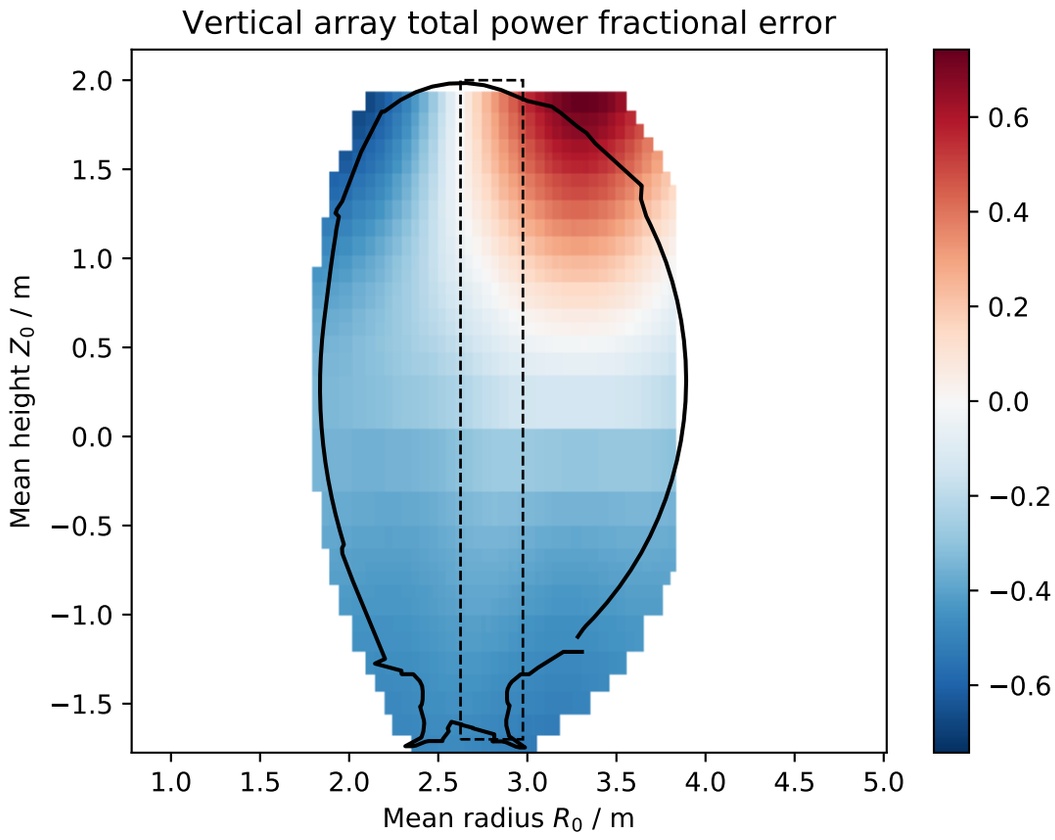

FIG. 8: The fractional error $(P_{ws} - P_{phantom})/P_{phantom}$ of the weighted sum P_{ws} and the total power calculated from phantoms $P_{phantom}$, as a function of the mean position of each phantom, using the vertical bolometer array (KB5V) and Gaussian phantoms. The total power is fairly consistently under-estimated, except at the top of the machine nearest the detectors (which also happens to be nearest to the SPI). The dashed box indicates that phantoms within this region produced synthetic brightness profiles similar to measured profiles.

horizontal array over-estimates the total power when the radiation is near the midplane and underestimates near the top and bottom of the device. The variation in the error is smaller and varies more slowly with position when using the horizontal array rather than the vertical array. These results appear consistent with the work of Sato et. al.[16], when we consider that the horizontal bolometer is at a smaller radius $R_{bol} = 5.05\,\mathrm{m}$ than the optimum radius for total radiated power calculations using a weighted sum: for JET this optimum radius would

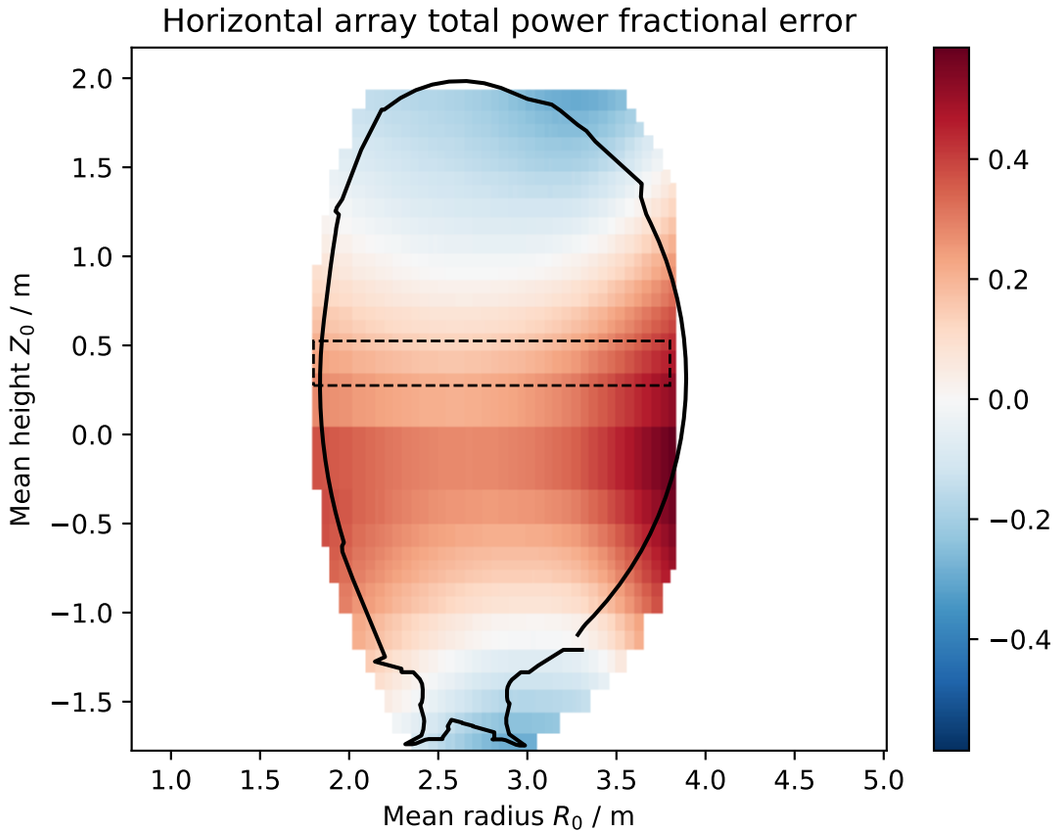

FIG. 9: The fractional error $(P_{ws} - P_{phantom})/P_{phantom}$ of the weighted sum P_{ws} and the total power calculated from phantoms $P_{phantom}$, as a function of the mean position of each phantom, using the horizontal bolometer array (KB5H) and Gaussian phantoms. The total power is overestimated near the midplane, but underestimated at the top and bottom of the device. The dashed box indicates that phantoms within this region produced synthetic brightness profiles similar to measured profiles.

be $R_{opt} = R_{\min} + R_{\max} = 5.73\,\mathrm{m}$ using the definition in that work[16].

Although consistent with previous work, the strong positional dependence of the total power calculated using the vertical array, and the weaker dependence when using the horizontal array, is not intuitive. It is in fact a consequence of the geometry of the bolometer arrays: the lines of sight are not parallel but fan out from a single point. The weighted sum method is only mathematically exact for parallel lines of sight, and the mapping from diverging to parallel lines of sight has a major impact on the weights used. This effect is

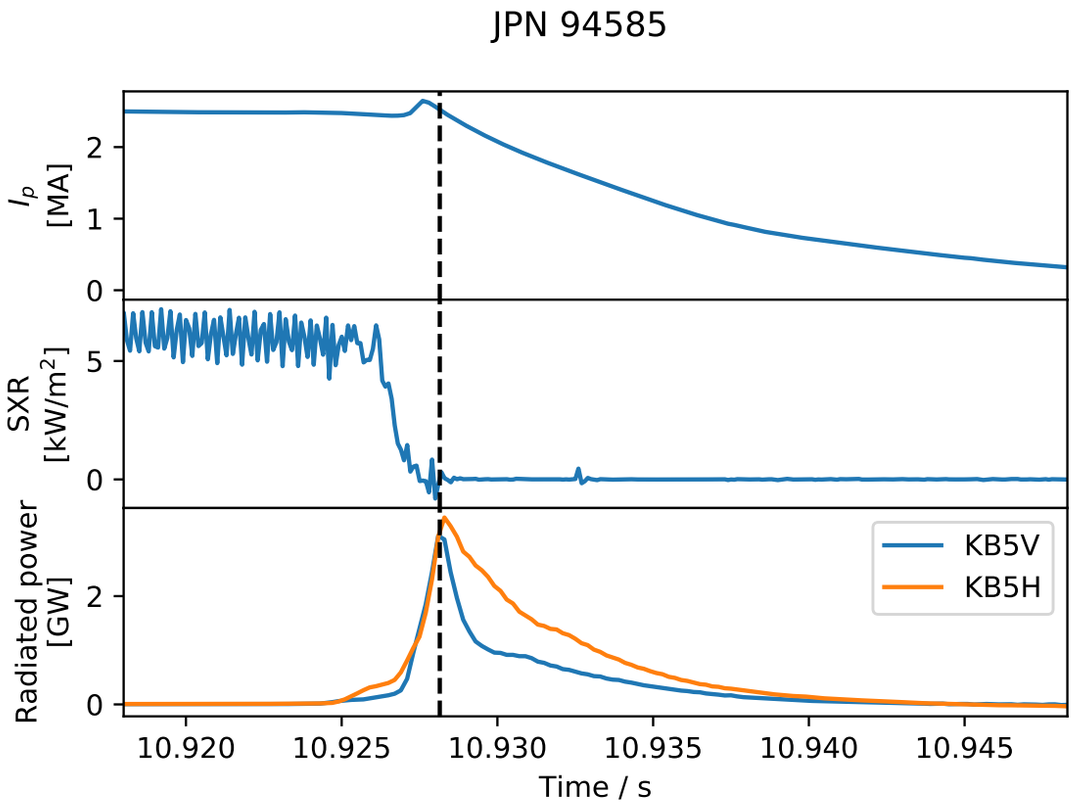

FIG. 10: Time histories of the plasma current, core soft X ray brightness and the total radiated power estimated from the weighted sum method for a typical SPI-mitigated disruption in JET.@ Neither of the KB5H or KB5V weighted sum calculations have had correction scale factors applied in this case, so quantitative comparison should be avoided. The dashed lines indicate the time at which the measured profiles were taken for comparison against synthetic brightness profiles from phantoms.

discussed in reference[12]: the reader is referred to that work for further details.

This 2D scan shows variations throughout the entire cross section of the device, but we are able to localise the radiation a bit better than this. The vertical bolometer array can constrain the radial position and extent of the radiation in its poloidal plane in Octant 3, and the horizontal bolometer array can constrain the vertical position and extent of the radiation in its poloidal plane in Octant 6. This allows us to estimate the range of systematic errors which could be present in measurements of SPI-mitigated disruptions in JET by choosing phantom shapes which reproduce the brightness profiles measured in JET disruptions. We chose a representative SPI-induced disruption, from JET pulse 94585 with $B_T = 2.5\,\mathrm{T}$,

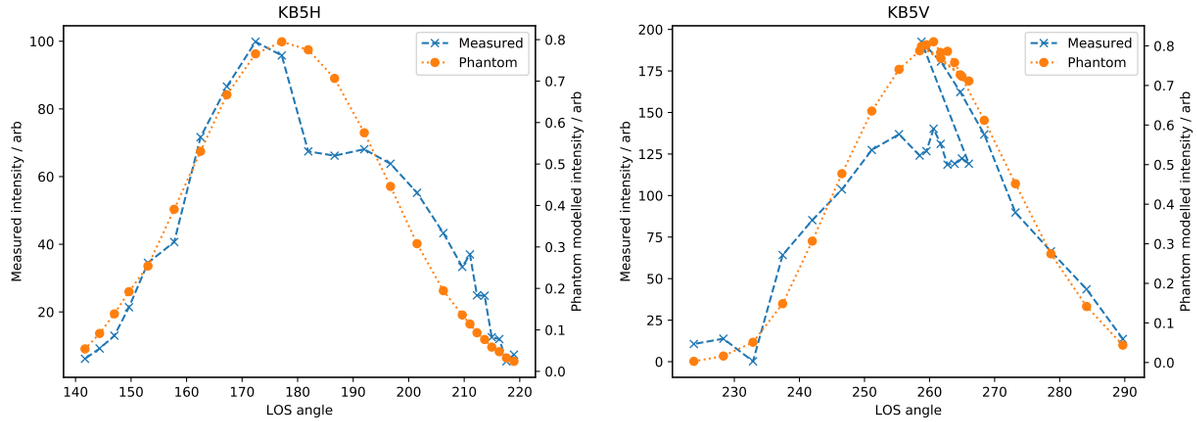

FIG. 11: The brightness profiles measured with the horizontal (left) and vertical (right) bolometer cameras for an SPI-mitigated disruption in JET, taken at the time slice shown in Figure 10. The LOS angle is defined as the angle between the line of sight vector and the positive R axis. Also shown are the synthetic brightness profiles from Gaussian phantoms which produce roughly the same measurements.

$I_p = 2.5\,\mathrm{MA}$ and $W_p = 4\,\mathrm{MJ}$, and measured the brightness profiles from both arrays at the time indicated in Figure 10.

The left plot in Figure 11 shows the brightness profile measured by the horizontal bolometer array. On the same plot is the forward-modelled horizontal bolometer brightness profile of a Gaussian phantom with $R_0 = 2.8\,\mathrm{m}$, $Z_0 = 0.38\,\mathrm{m}$, $\delta R = 0.2\,\mathrm{m}$ and $\delta Z = 0.5\,\mathrm{m}$, which produces a similar profile. Although the R_0 and δR values of the phantom are unconstrained by the horizontal array, the profile shows which Z_0 and δZ values are applicable to the measured power. The same analysis can be performed for the vertical array, to determine which values of R_0 and δR are most relevant to the investigation. The right plot in Figure 11 shows a comparison of the measured brightness profile from the vertical array, at the same time slice in Figure 10, with a Gaussian phantom specified by $R_0 = 2.8\,\mathrm{m}$, $Z_0 = 0.38\,\mathrm{m}$, $\delta R = 0.5\,\mathrm{m}$ and $\delta Z = 0.5\,\mathrm{m}$. Note that there are some discrepancies in the finer details of the shape of these profiles, such as the enhanced radiation in the lower part of the vessel measured by the horizontal array and the reduction in brightness measured by the narrow divertor-viewing channels at angles 258° to 266° compared with the wider-angle channels at similar angles: this is because the real emissivity profiles are not actually Gaussian but a different (unknown) shape. The dashed boxes in Figures 8 and 9 indicate phantoms with (R_0, Z_0)

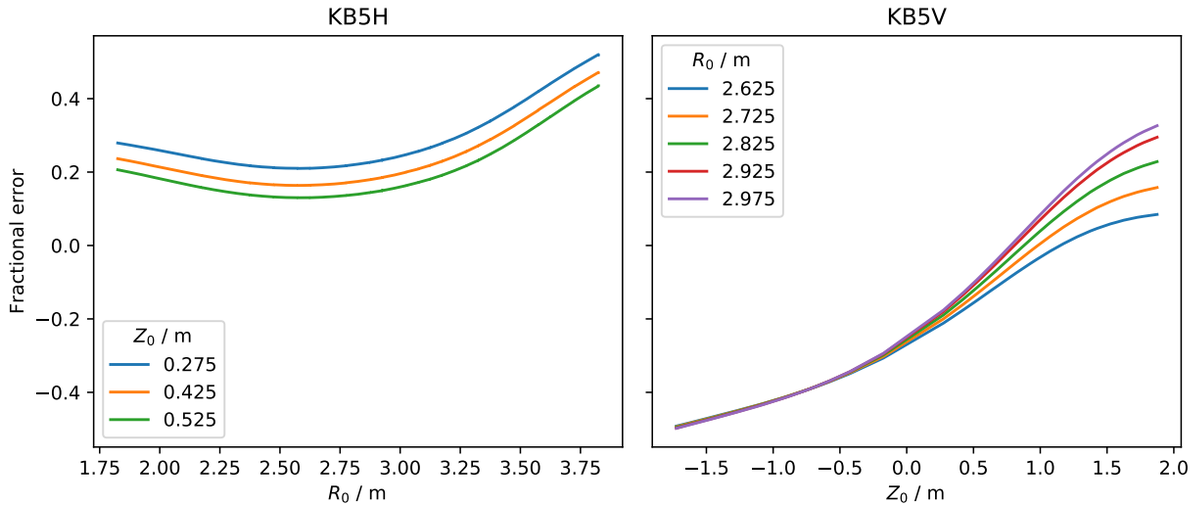

FIG. 12: The fractional error $(P_{ws} - P_{phantom})/P_{phantom}$ of the weighted sum of the horizontal (left) and vertical (right) bolometer channels and the total power calculated from phantoms with Z_0 and δZ (left) or R_0 and δR (right) values which produce brightness profiles similar to those measured during disruptions, as a function of mean phantom position. The systematic error in the horizontal array is less sensitive to horizontal position than the systematic error in the vertical array is to vertical position.

values which produced synthetic brightness profiles similar to these measured profiles.

The right hand plot of Figure 12 shows this subset of results from Figure 8, where we have restricted the analysis to values of R_0 and δR which produce brightness profiles similar to what are measured in experiments. Since the lines of sight are not completely vertical, there are a few different R_0 values which are suitable. We see a large variation in the systematic error as a function of vertical position, which is unconstrained by the vertical bolometer measurements. Near the top of the vessel (close to the bolometers) there is also significant variation with changing R_0. We therefore see that if only the weighted sum of the vertical bolometer channels is used to estimate the total radiated power, the uncertainty is of the order of 70%. Use of predictive 3D modelling to estimate the position of the radiation at the toroidal location of the KB5V bolometers may reduce this uncertainty. Nevertheless, it is clear that the weighted sum of the vertical channels alone will not provide an accurate-enough estimate of the radiated power to confirm the SPI achieves the $> 95\%$ radiated fraction required for ITER, and could also suggest trends in the calculated radiation

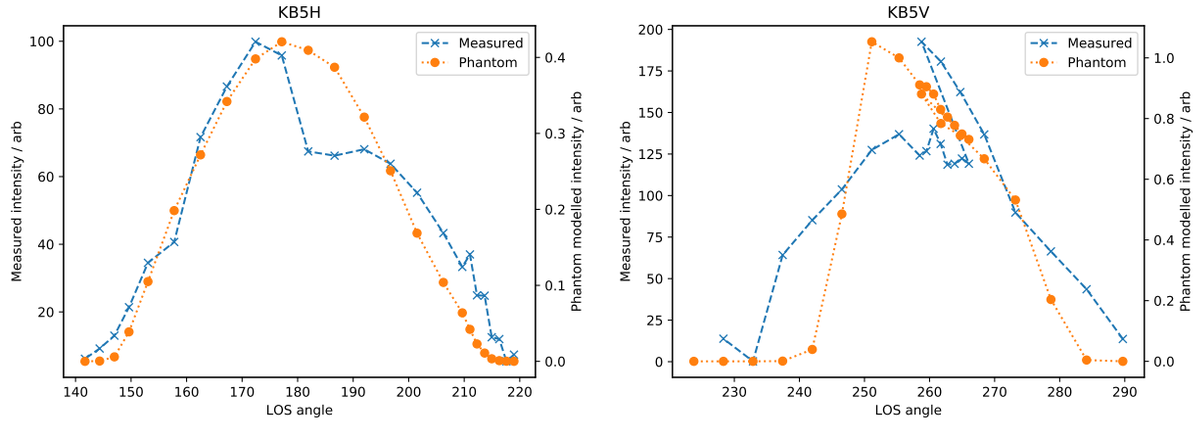

FIG. 13: Comparison of synthetic and measured brightness profiles, as in Figure 11, this time using flux-aligned phantoms.

fraction which are not real if there is variation in the vertical position of the radiation.

The left hand plot of Figure 12 shows the same analysis for the horizontal array, restricting Z_0 and δZ to values which produce synthetic brightness profiles similar to those measured. This looks more promising: the fractional error varies more slowly with changing R_0 than the corresponding change in Z_0 in the vertical array. In fact, there is a reasonably large window in major radius where there is only a 10% variation in the systematic error, and this is true for the range of R_0 values which match measured profiles. This suggests that with a suitable scaling factor of $\sim 1/1.2$ applied to the horizontal weighted sum, we can confidently estimate the radiated power in the poloidal plane of the horizontal bolometers in Octant 6 to within about 10%.

It is important to emphasise that we are not suggesting this translates to an error of 10% on the total radiated power in the entire plasma volume. There is still an uncertainty in the toroidal variation of the radiation, both in the magnitude of the variation and the phase of the variation in Octant 6 (i.e. whether the toroidal component of the radiation is near a maximum or a minimum at this toroidal location). Using modelling and field-line tracing to predict more accurately where the radiation is likely to be peaked, along with analysis of the KB1 data described in Section II, could reduce this error further. The work we present here provides an estimate of the uncertainty in the radiated power in the poloidal plane of the bolometers only, with the aim of avoiding false precision by applying the standard bolometer analysis techniques used for non-disrupting JET plasmas.

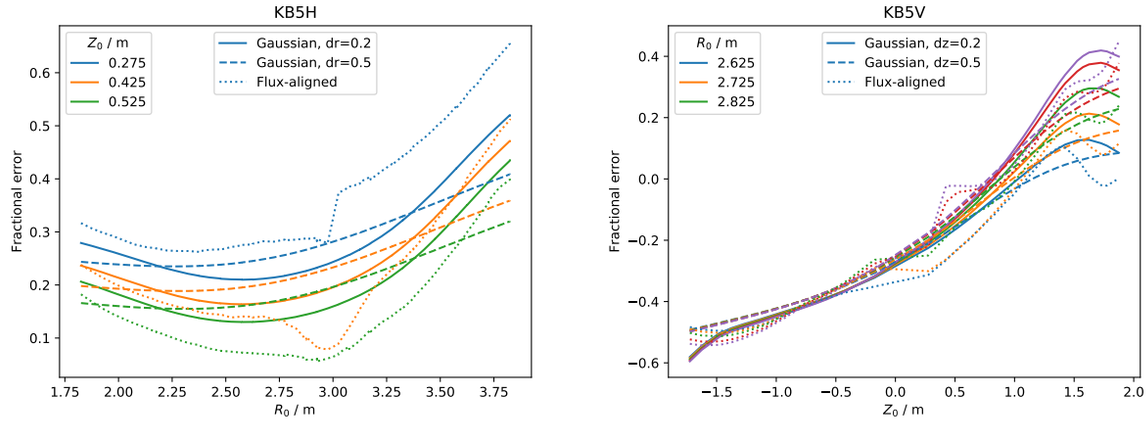

FIG. 14: The ratio of the weighted sum of the horizontal (left) and vertical (right) bolometer channels and the total power calculated from phantoms of different shapes and sizes. The trend in the systematic error is similar for both sizes of Gaussian phantoms and for flux-aligned phantoms, for both arrays.

So far we have presented results using only Gaussian phantoms, with a single value of $\delta Z = 0.5\,\mathrm{m}$ (for the vertical array) and $\delta R = 0.2\,\mathrm{m}$ (for the horizontal array). Figure 14 shows the results of performing the same analysis for phantoms of different shapes: Gaussian phantoms of height $\delta Z = 0.5\,\mathrm{m}$ and widths $\delta R = 0.2\,\mathrm{m}$ and $0.5\,\mathrm{m}$ for the horizontal array, and width $\delta R = 0.5\,\mathrm{m}$ and heights $\delta Z = 0.2\,\mathrm{m}$ and $0.5\,\mathrm{m}$ for the vertical array, and also flux aligned phantoms defined in flux coordinates with widths $\delta\psi_n = 0.1$ and $\delta\beta = 0.5\,\mathrm{rad}$ for both arrays. The ψ_0 and β_0 values of the flux aligned phantoms were chosen such that the mean position of these phantoms in R, Z space was similar to that of the Gaussian phantoms, to provide a meaningful comparison.

Figure 13 shows a comparison of the measured profiles with synthetic profiles obtained with representative flux aligned phantoms defined by $\psi_0 = 0.8$, $\beta_0 = 0.1\,\mathrm{rad}$, $\delta\psi = 0.1$ and $\delta\beta = 0.5\,\mathrm{rad}$ for the KB5H comparison, and $\psi_0 = 0.45$, $\beta_0 = 1.65\,\mathrm{rad}$, $\delta\psi = 0.1$ and $\delta\beta = 0.5\,\mathrm{rad}$ for the KB5V comparison. As in the Gaussian phantom case shown in Figure 11, these flux-aligned phantoms produce brightness profiles with similar overall position and width to the measured profiles but differ in the finer details of the profile shape. The qualitative agreement is similar to the Gaussian phantoms for KB5H but slightly worse than the Gaussian phantoms for the KB5V case. Note that because the shape of the flux-aligned phantoms changes significantly (particularly around the magnetic axis) the degree of

discrepancy in the shape varies. For brevity we have only shown two cases in Figure 13: the degree of discrepancy is similar for the other flux-aligned phantoms analysed in Figure 14.

The Gaussian phantom trends for the two different radial widths are qualitatively and quantitatively similar. Even the flux aligned phantoms show similar trends, despite the shape in R, Z space varying substantially across the magnetic equilibrium, especially near to the magnetic axis at $(R, Z) = (3.0\,\mathrm{m}, 0.3\,\mathrm{m})$: phantoms whose shapes produce different degrees of disagreement in the detailed shape of the brightness profiles compared with measured profiles still exhibit the same variation in fractional error with phantom position. These results suggest it is really the mean position of the radiation which has the strongest effect on the systematic error in the power calculated using the weighted sum method. As such, we expect the suggested scaling factor of 1/1.2 to the total power calculated using the horizontal array will be suitable for a wide range of phantom shapes and sizes, provided they qualitatively match the measured profiles. For the vertical array a single scaling factor does not exist, as the variation with position of the radiation is much larger. The weak dependence of systematic error on phantom shape also justifies our use of phantoms with emissivity profiles in moderate but not exact agreement with the detailed shape of measured profiles.

IV. CONCLUSION

A methodology has been developed to quantify the systematic uncertainty when using a weighted sum of the JET vertical or horizontal bolometer channels to estimate the total radiated power at two different toroidal locations. While both span the plasma cross section and see the entire plasma, each will have a different total radiated power estimate when the radiation is toroidally or poloidally localised. We find that the vertical bolometer system has a systematic error which is very sensitive to the (unconstrained) vertical position of the radiation, resulting in large uncertainties on the total power calculation. The horizontal bolometer is less sensitive to the (unconstrained) radial position of the radiation, and so provides a more reliable estimate of the total radiated power at the toroidal location of the array. We show that the weighted sum of these horizontal bolometer channels over-estimates the total power by between 15% and 30%, and so a correction factor of approximately 1/1.2 should be applied to the methods described in[12] to get the correct power in the particular

poloidal plane of the bolometer array with an uncertainty in the region of 10%.

We have also described the use of 4 toroidal single-channel bolometers to provide evidence of radiation asymmetries in SPI-mitigated disruptions. A new analysis approach was shown to overcome noisy signals and the lack of an in-situ calibration method. We are able to quantify the energy radiated during a disruption in 4 identical poloidal regions in different toroidal locations inside JET. This has uncovered some noticeable patterns, including that the toroidal radiation peaking at the LFS is observed to increase as the amount of neon used in the pellets increases for plasmas with the same thermal energy.

With these two new methods for radiated power analysis in JET, we can better constrain estimates of the total radiated power during disruptions. We have provided tools to quantify the uncertainties due to both the poloidal distribution of the radiation used in weighted sum calculations of the total power, and also due to toroidal asymmetries in the radiation. With this improved uncertainty quantification we can avoid misinterpreting apparent trends in the calculation of the total radiated power: rather than real variations, trends may instead be a diagnostic effect.

It must be noted that there are fundamental limitations to the information the existing JET bolometer diagnostics can provide towards quantifying the fraction of stored energy which is radiated during SPI-mitigated disruptions. Full poloidal coverage is only availble in two toroidal locations, and the toroidal asymmetry can only be measured on the low field side: the high field side asymmetry is unconstrained by the bolometer diagnostics. The use of data from JET's bolometer systems alone will not be sufficient to confidently assess whether the SPI system is capable of the >95% radiation fractions required for ITER. In the short term, modelling which predicts both the radiation fraction and 3D emissivity profiles may improve this, and the bolometer measurements will be an important verification of these models. The techniques outlined here could inform upgrades of the bolometer diagnostic suite at JET to further improve confidence in the SPI system's effectiveness and suitability for ITER.

ACKNOWLEDGEMENTS

This work has been supported by DOE under DE-AC05-00OR22725. This work has been carried out within the framework of the EUROfusion Consortium and has received funding

from the Euratom research and training programme 2014–2018 and 2019–2020 under grant agreement No 633053. The views and opinions expressed herein do not necessarily reflect those of the European Commission.

DATA AVAILABILITY

Raw data were generated at the JET large scale facility. Derived data supporting the findings of this study are available from the corresponding author upon reasonable request.

REFERENCES

[1]V. Riccardo, G. Arnoux, P. Cahyna, T. C. Hender, A. Huber, S. Jachmich, V. Kiptily, R. Koslowski, L. Krlin, M. Lehnen, A. Loarte, E. Nardon, R. Paprok, and D. T. and, Plasma Physics and Controlled Fusion **52**, 124018 (2010).

[2]E. M. Hollmann, P. B. Aleynikov, T. Fülöp, D. A. Humphreys, V. A. Izzo, M. Lehnen, V. E. Lukash, G. Papp, G. Pautasso, F. Saint-Laurent, and J. A. Snipes, Physics of Plasmas **22**, 021802 (2015), https://doi.org/10.1063/1.4901251.

[3]L. Baylor, S. Meitner, T. Gebhart, J. Caughman, J. Herfindal, D. Shiraki, and D. Youchison, Nuclear Fusion **59**, 066008 (2019).

[4]V. A. Izzo, Physics of Plasmas **20**, 056107 (2013), https://doi.org/10.1063/1.4803896.

[5]A. Huber, K. McCormick, P. Andrew, P. Beaumont, S. Dalley, J. Fink, J. Fuchs, K. Fullard, W. Fundamenski, L. Ingesson, F. Mast, S. Jachmich, G. Matthews, P. Mertens, V. Philipps, R. Pitts, S. Sanders, and W. Zeidner, Fusion Engineering and Design **82**, 1327 (2007), proceedings of the 24th Symposium on Fusion Technology.

[6]M. Reinke, D. Whyte, R. Granetz, and I. Hutchinson, Nuclear Fusion **48**, 125004 (2008).

[7]G. Olynyk, R. Granetz, M. Reinke, D. Whyte, T. Golfinopoulos, J. Hughes, J. Walk, V. Izzo, S. Combs, S. Milora, and M. Brookman, Nuclear Fusion **53**, 092001 (2013).

[8]M. Lehnen, S. Gerasimov, S. Jachmich, H. Koslowski, U. Kruezi, G. Matthews, J. Mlynar, C. Reux, P. de Vries, *et al.*, Nuclear fusion **55**, 123027 (2015).

[9]K. F. Mast, H. Krause, K. Behringer, A. Bulliard, and G. Magyar, Review of Scientific Instruments **56**, 969 (1985), https://doi.org/10.1063/1.1138007.

[10]K. F. Mast, J. C. Vallet, C. Andelfinger, P. Betzler, H. Kraus, and G. Schramm, Review of Scientific Instruments **62**, 744 (1991), https://doi.org/10.1063/1.1142078.

[11]J. Lovell, "Development of smart, compact fusion diagnostics using field-programmable gate arrays," (2017), section 3.1.3. PhD Thesis.

[12]L. C. Ingesson, "Comparison of methods to determine the total radiated power in JET," JET technical report JET-R(99)06 (JET Joint Undertaking, 1999).

[13]C. Giroud, A. Meakins, M. Carr, A. Baciero, and C. Bertrand, "Cherab spectroscopy modelling framework," (2019).

[14]G. Huysmans and O. Czarny, Nuclear Fusion **47**, 659 (2007).

[15]N. Ferraro, B. Lyons, C. Kim, Y. Liu, and S. Jardin, Nuclear Fusion **59**, 016001 (2018).

[16]R. Sano, M. Fukumoto, T. Nakano, and N. Oyama, Review of Scientific Instruments **89**, 083501 (2018), https://doi.org/10.1063/1.5026927.

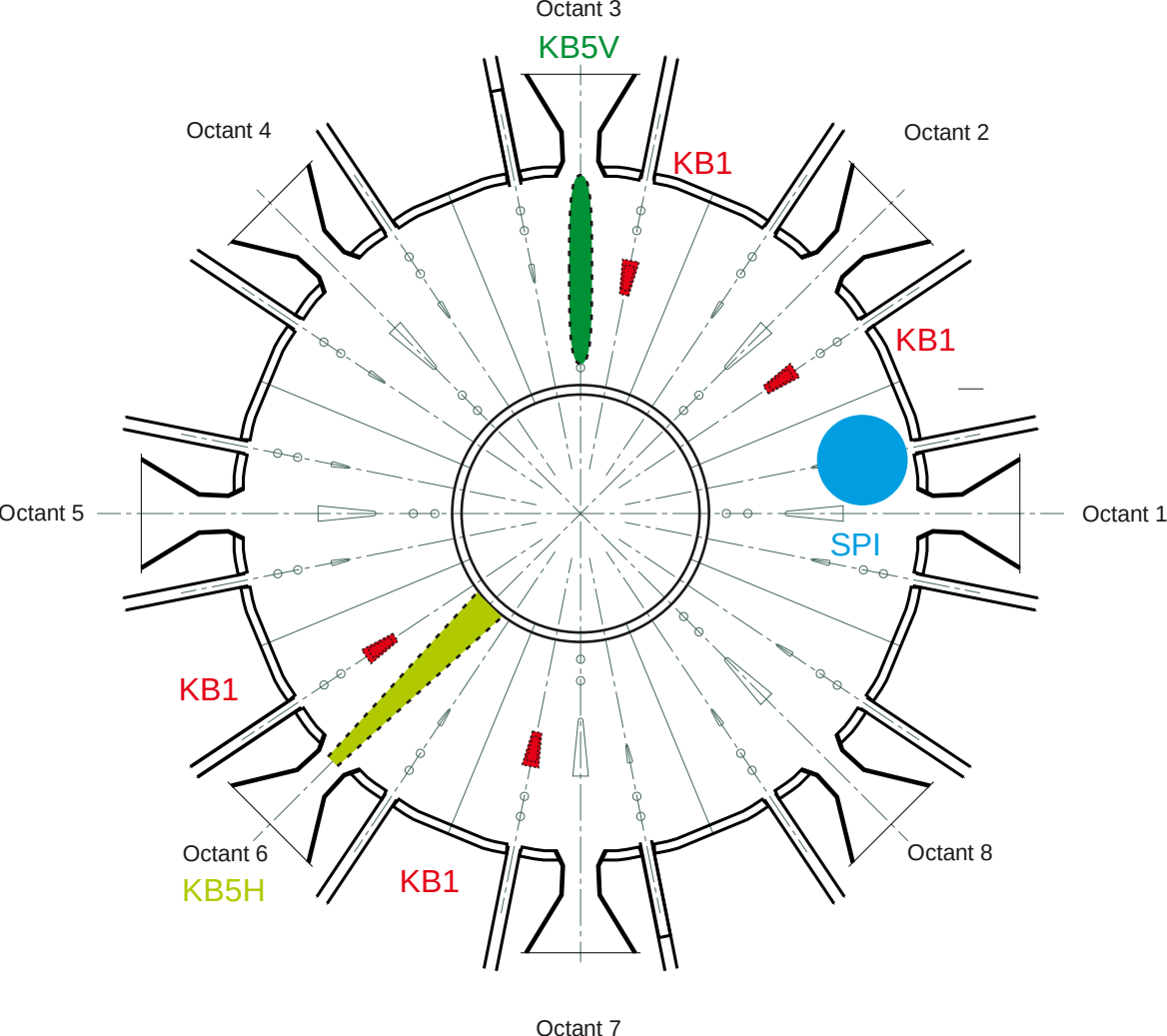
Octant 3
KB5V
Octant 4
KB1
Octant 2
KB1
Octant 5
Octant 1
SPI
KB1
Octant 6
KB5H
KB1
Octant 8
Octant 7

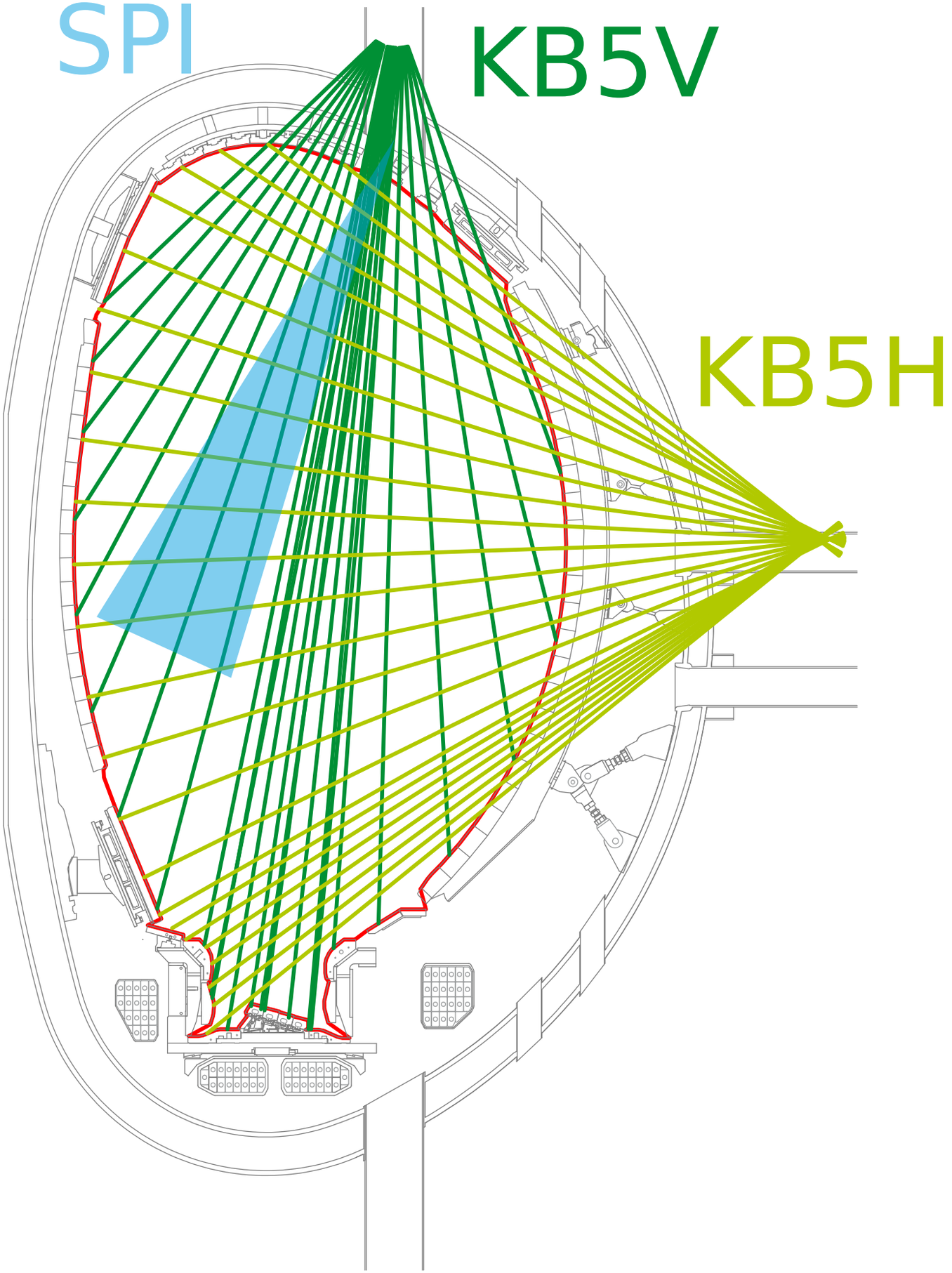
SPI
KB5V
KB5H

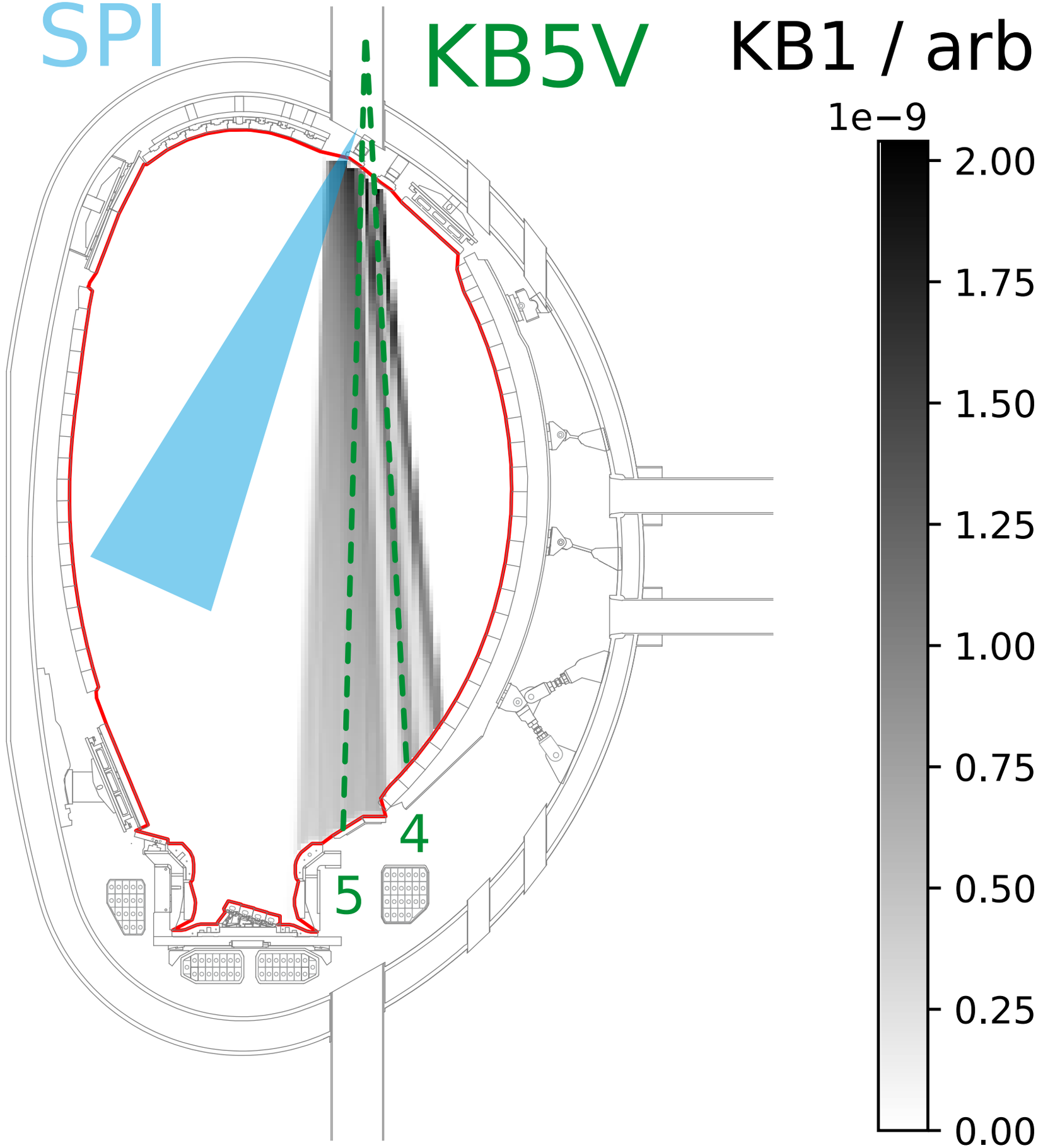
SPI
KB5V
KB1 / arb
1e−9
2.00
1.75
1.50
1.25
1.00
0.75
0.50
0.25
0.00
4
5

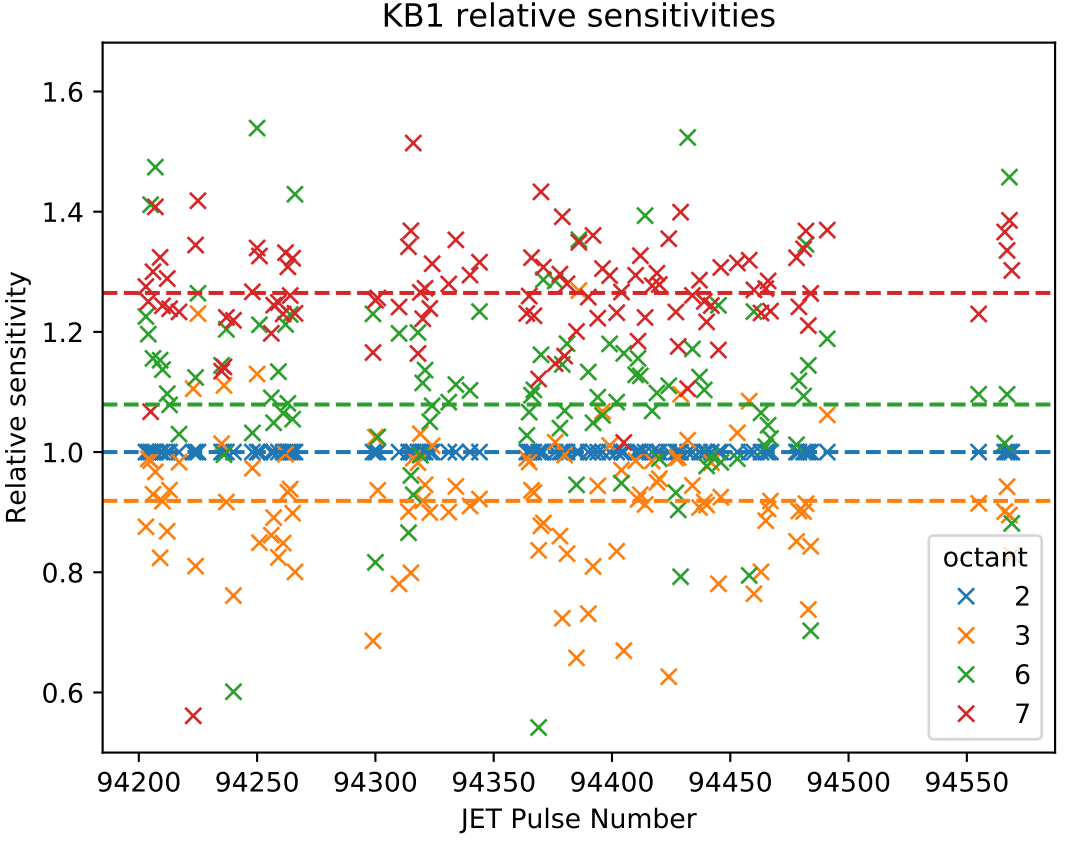
KB1 relative sensitivities
Relative sensitivity
1.6
1.4
1.2
1.0
0.8
0.6
94200
94250
94300
94350
94400
94450
94500
94550
JET Pulse Number
octant
2
3
6
7

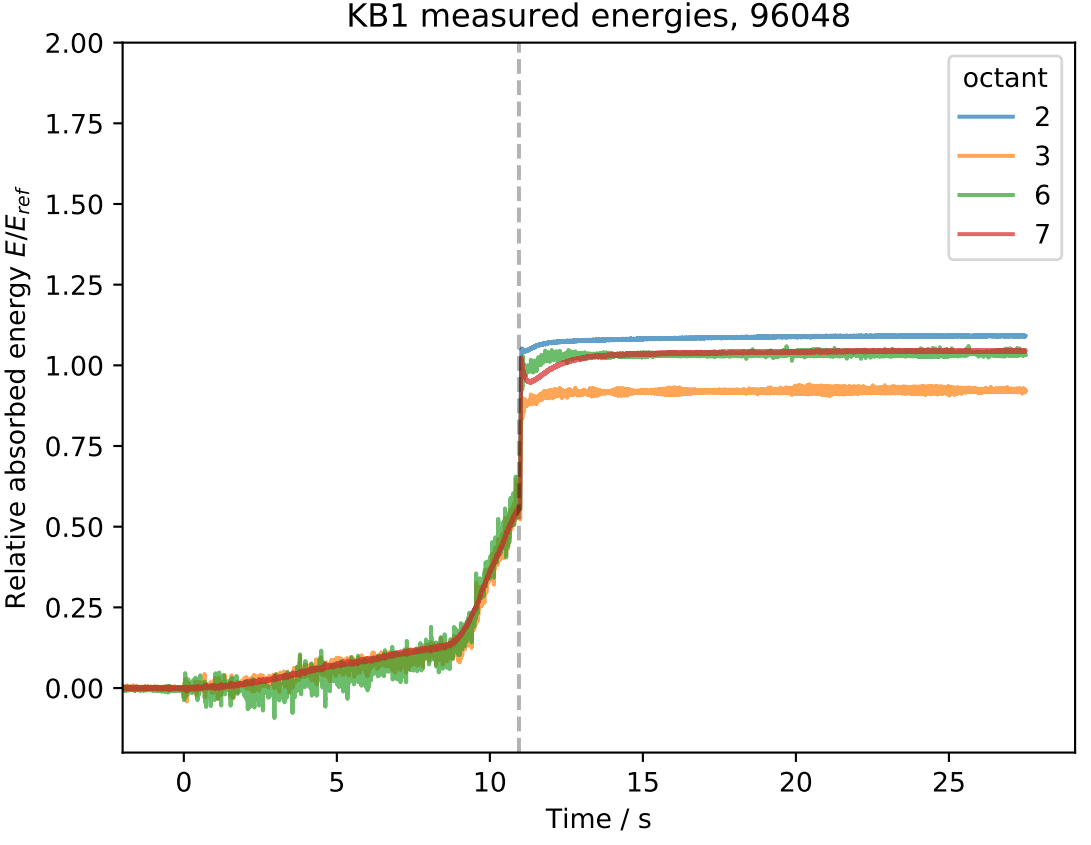
KB1 measured energies, 96048
Relative absorbed energy E/E_{ref}
Time / s
octant
2
3
6
7
2.00
1.75
1.50
1.25
1.00
0.75
0.50
0.25
0.00
0
5
10
15
20
25

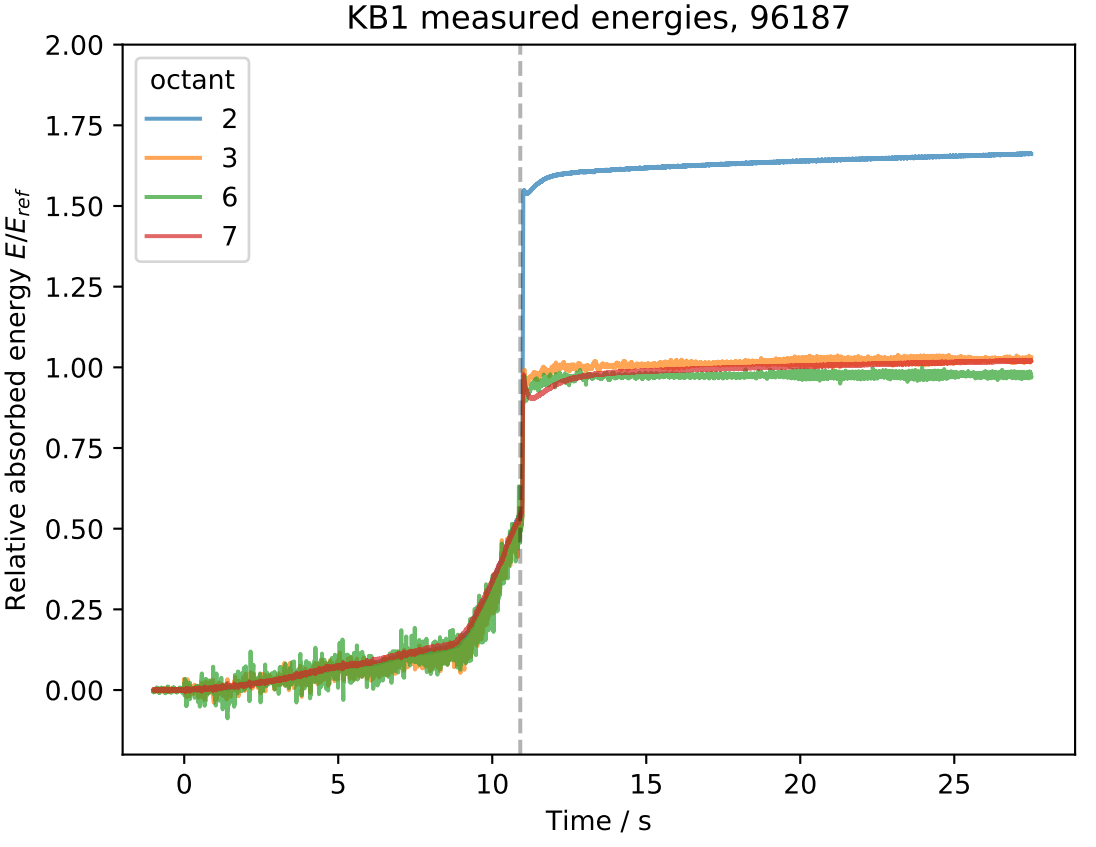
KB1 measured energies, 96187
octant
2
3
6
7
Relative absorbed energy E/E_{ref}
2.00
1.75
1.50
1.25
1.00
0.75
0.50
0.25
0.00
0
5
10
15
20
25
Time / s

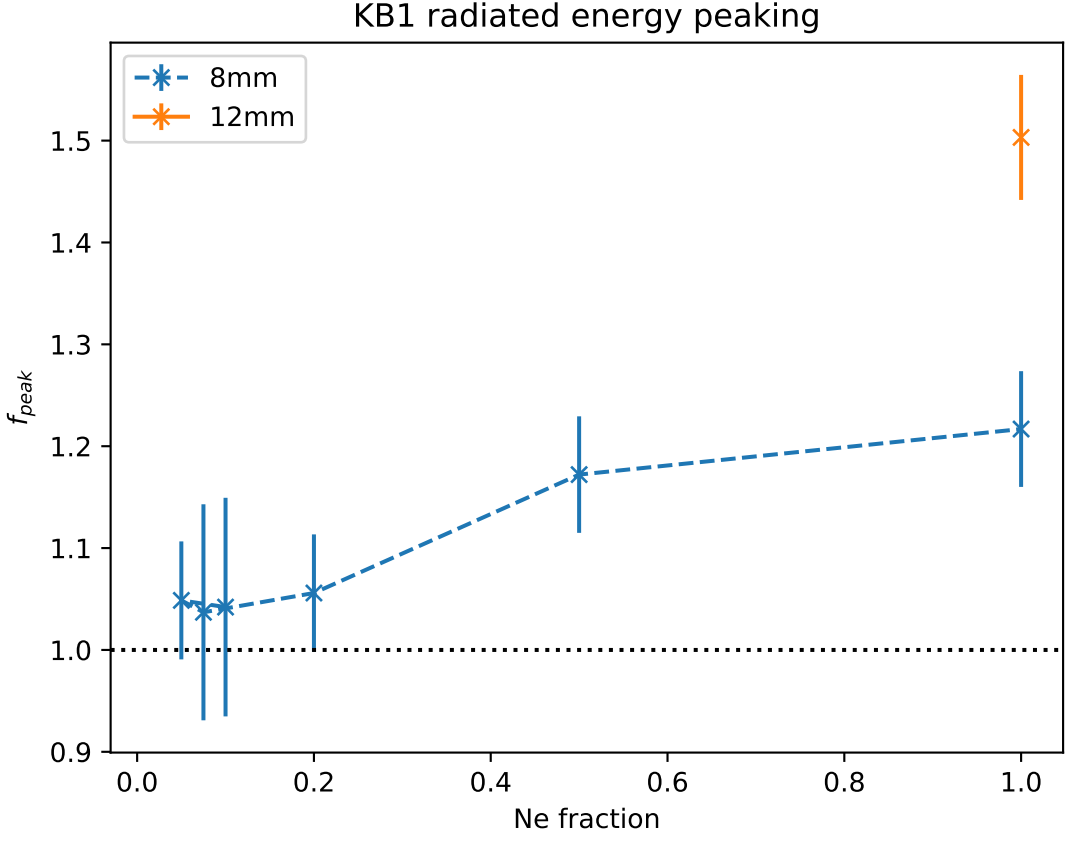
KB1 radiated energy peaking
8mm
12mm
1.5
1.4
1.3
1.2
1.1
1.0
0.9
f_{peak}
0.0
0.2
0.4
0.6
0.8
1.0
Ne fraction

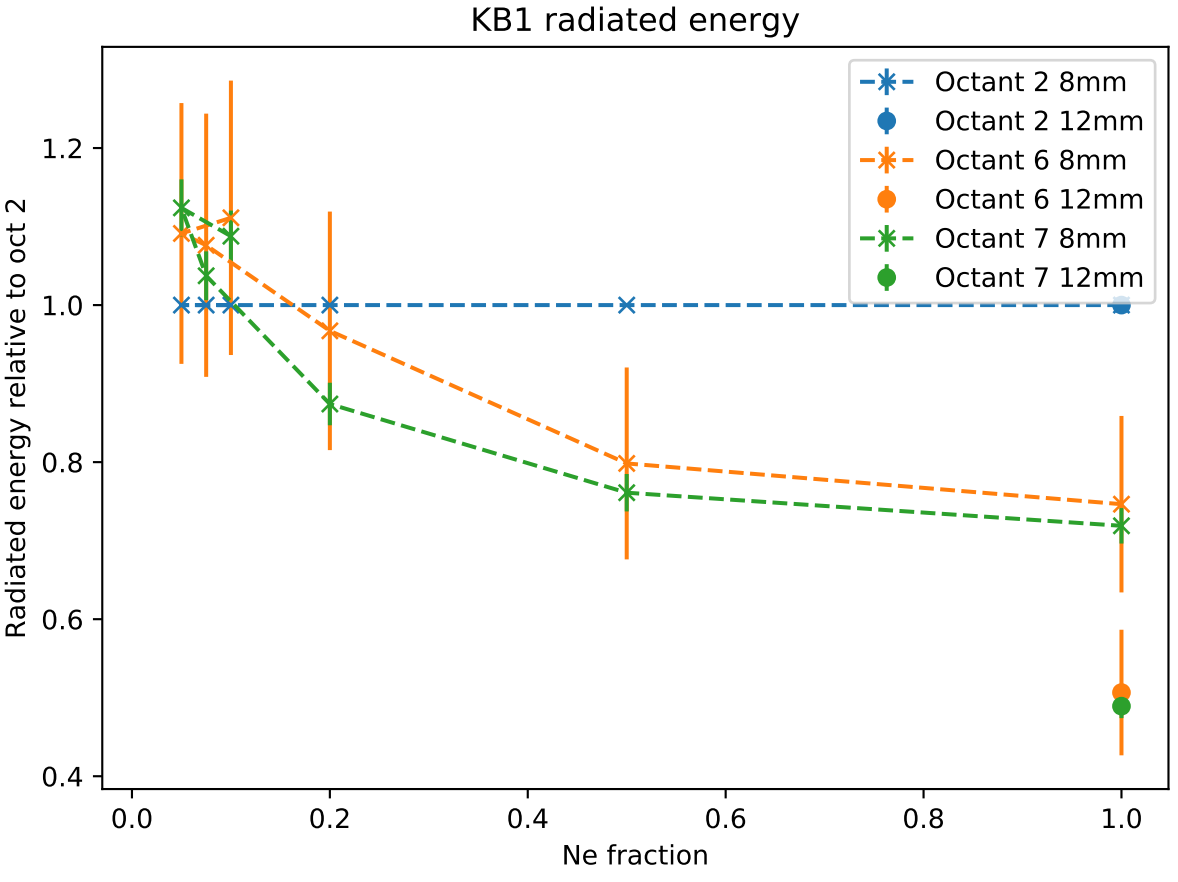
KB1 radiated energy
Octant 2 8mm
Octant 2 12mm
Octant 6 8mm
Octant 6 12mm
Octant 7 8mm
Octant 7 12mm
Radiated energy relative to oct 2
Ne fraction
0.4
0.6
0.8
1.0
1.2
0.0
0.2
0.4
0.6
0.8
1.0

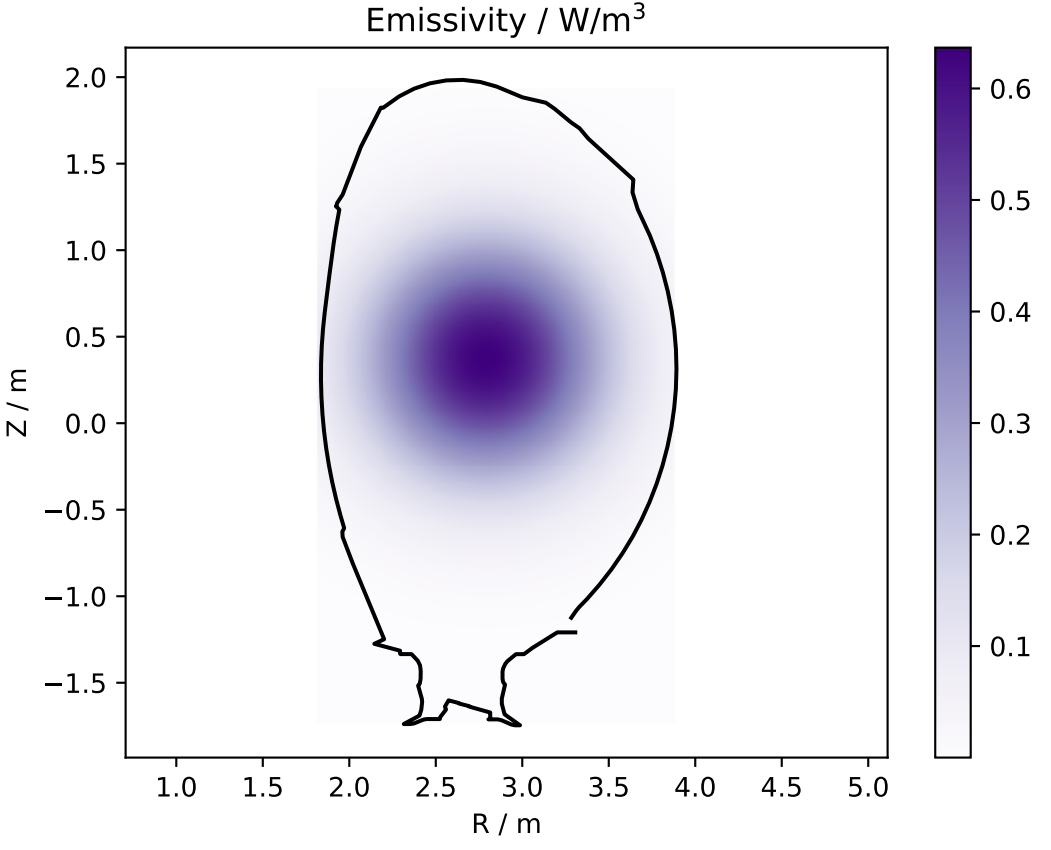
Emissivity / W/m^3
2.0
1.5
1.0
0.5
0.0
−0.5
−1.0
−1.5
Z / m
1.0
1.5
2.0
2.5
3.0
3.5
4.0
4.5
5.0
R / m
0.6
0.5
0.4
0.3
0.2
0.1

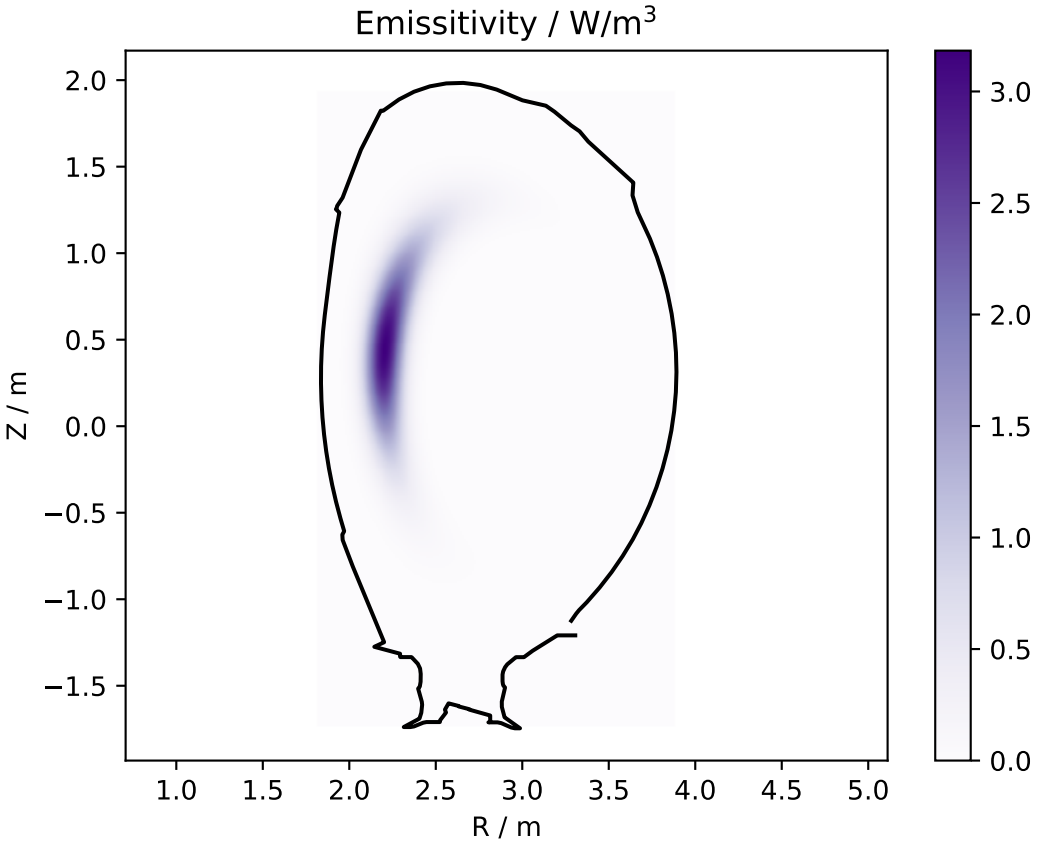
Emissitivity / W/m^3
2.0
1.5
1.0
0.5
0.0
−0.5
−1.0
−1.5
Z / m
1.0
1.5
2.0
2.5
3.0
3.5
4.0
4.5
5.0
R / m
3.0
2.5
2.0
1.5
1.0
0.5
0.0

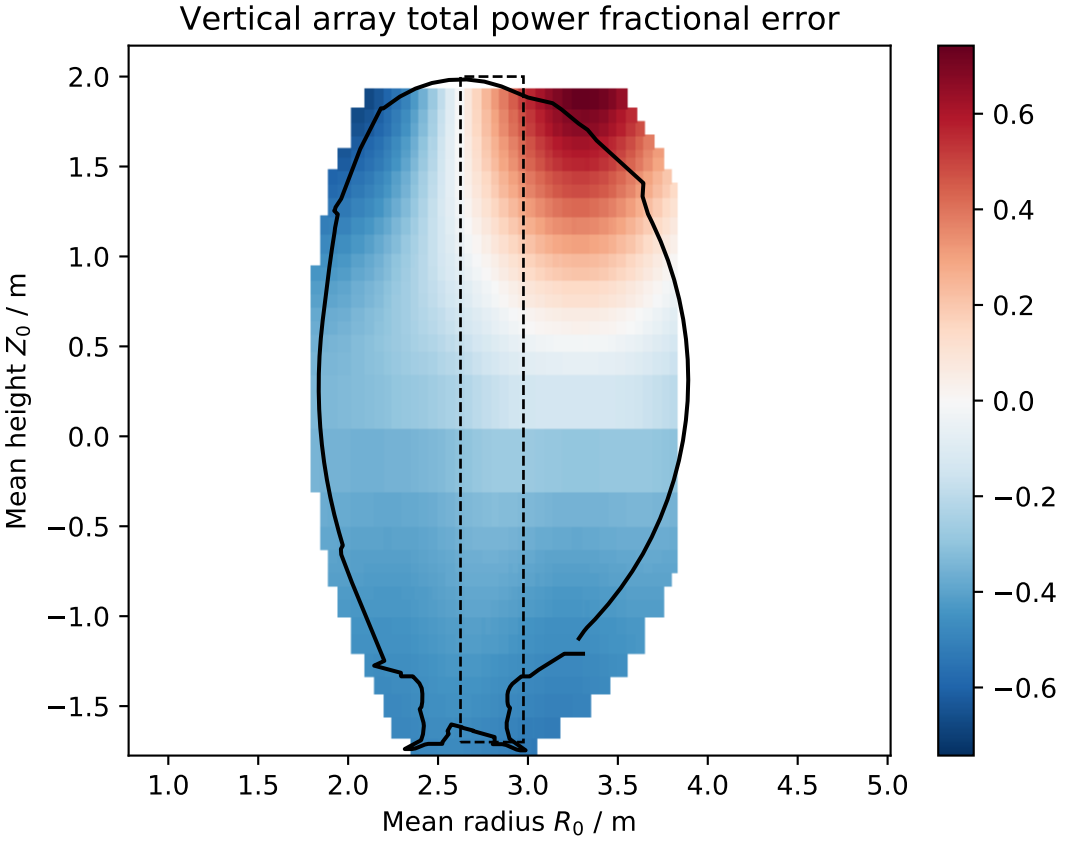
Vertical array total power fractional error
Mean height Z_0 / m
Mean radius R_0 / m
2.0
1.5
1.0
0.5
0.0
−0.5
−1.0
−1.5
1.0
1.5
2.0
2.5
3.0
3.5
4.0
4.5
5.0
0.6
0.4
0.2
0.0
−0.2
−0.4
−0.6

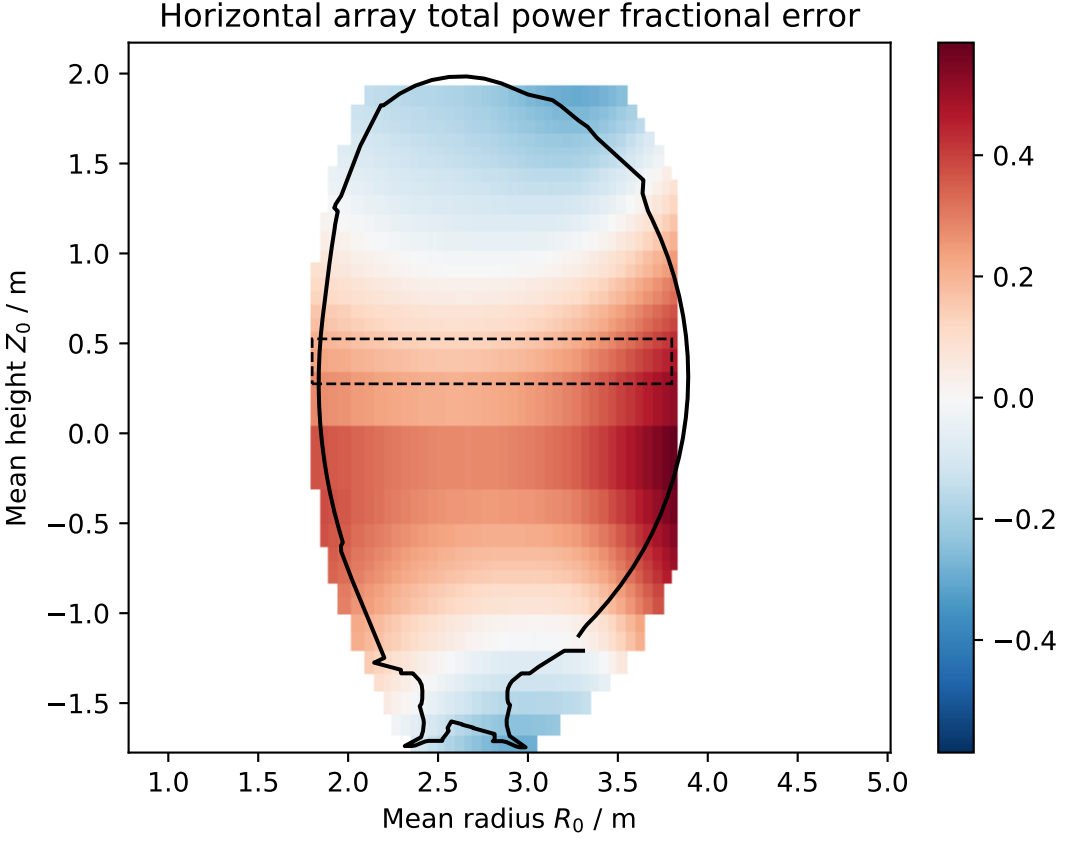
Horizontal array total power fractional error
Mean height Z_0 / m
Mean radius R_0 / m
2.0
1.5
1.0
0.5
0.0
−0.5
−1.0
−1.5
1.0
1.5
2.0
2.5
3.0
3.5
4.0
4.5
5.0
0.4
0.2
0.0
−0.2
−0.4

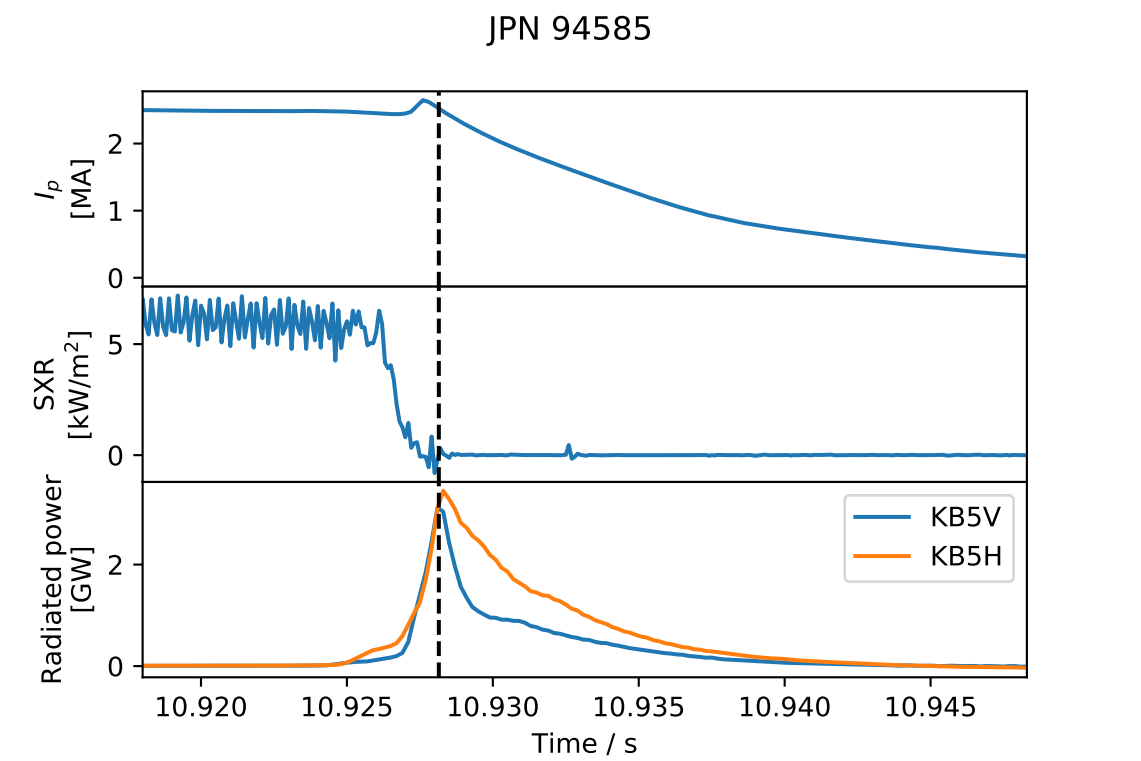
JPN 94585
I_p [MA]
SXR [kW/m^2]
Radiated power [GW]
KB5V
KB5H
Time / s
10.920
10.925
10.930
10.935
10.940
10.945

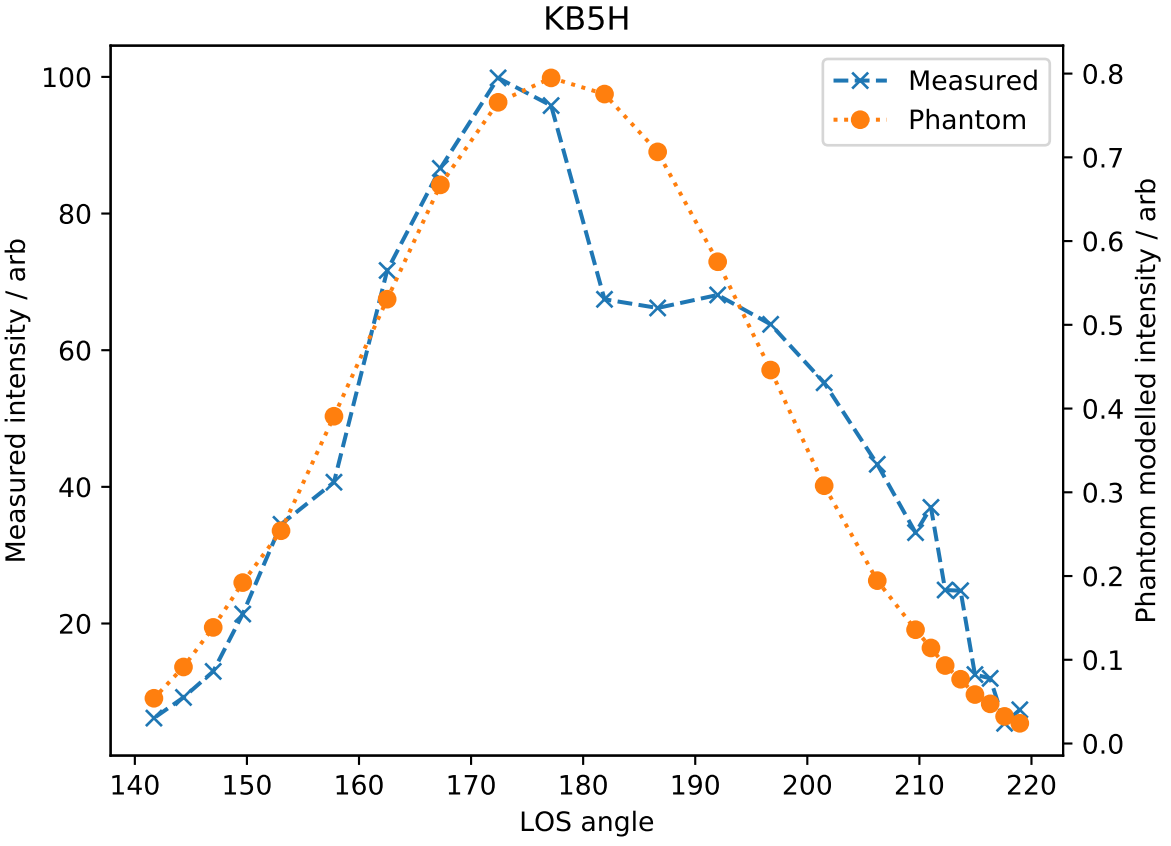
KB5H
Measured
Phantom
Measured intensity / arb
Phantom modelled intensity / arb
LOS angle
100
80
60
40
20
0.8
0.7
0.6
0.5
0.4
0.3
0.2
0.1
0.0
140
150
160
170
180
190
200
210
220

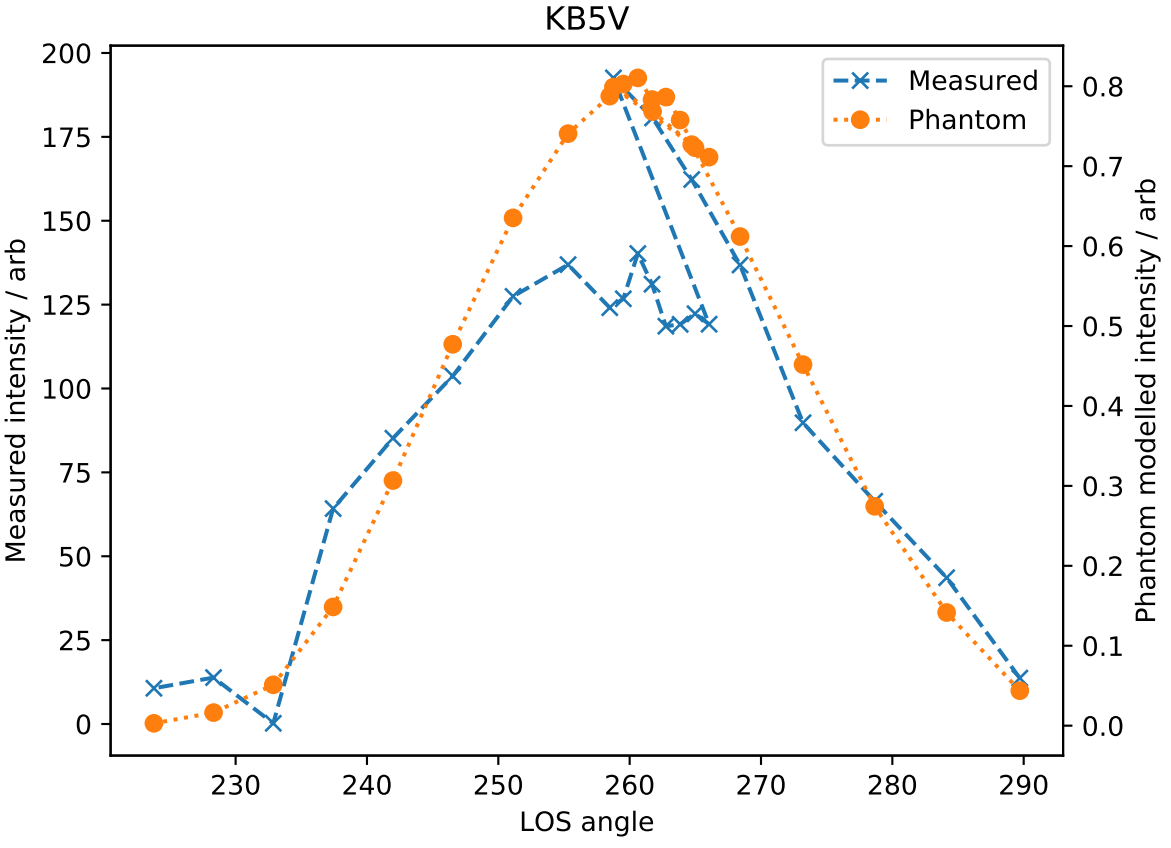
KB5V
Measured
Phantom
Measured intensity / arb
Phantom modelled intensity / arb
LOS angle
200
175
150
125
100
75
50
25
0
0.8
0.7
0.6
0.5
0.4
0.3
0.2
0.1
0.0
230
240
250
260
270
280
290

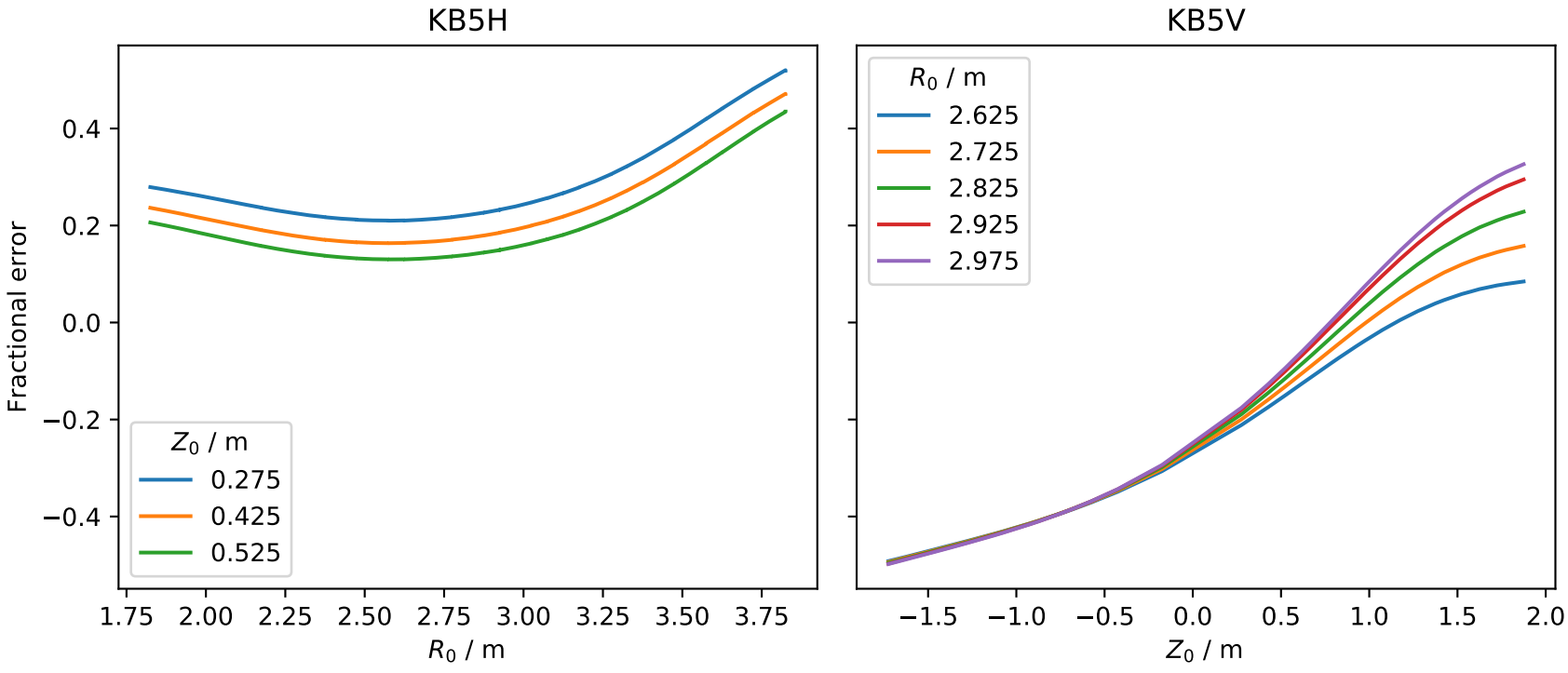
KB5H
KB5V
Fractional error
0.4
0.2
0.0
−0.2
−0.4
Z_0 / m
0.275
0.425
0.525
1.75
2.00
2.25
2.50
2.75
3.00
3.25
3.50
3.75
R_0 / m
R_0 / m
2.625
2.725
2.825
2.925
2.975
−1.5
−1.0
−0.5
0.0
0.5
1.0
1.5
2.0
Z_0 / m

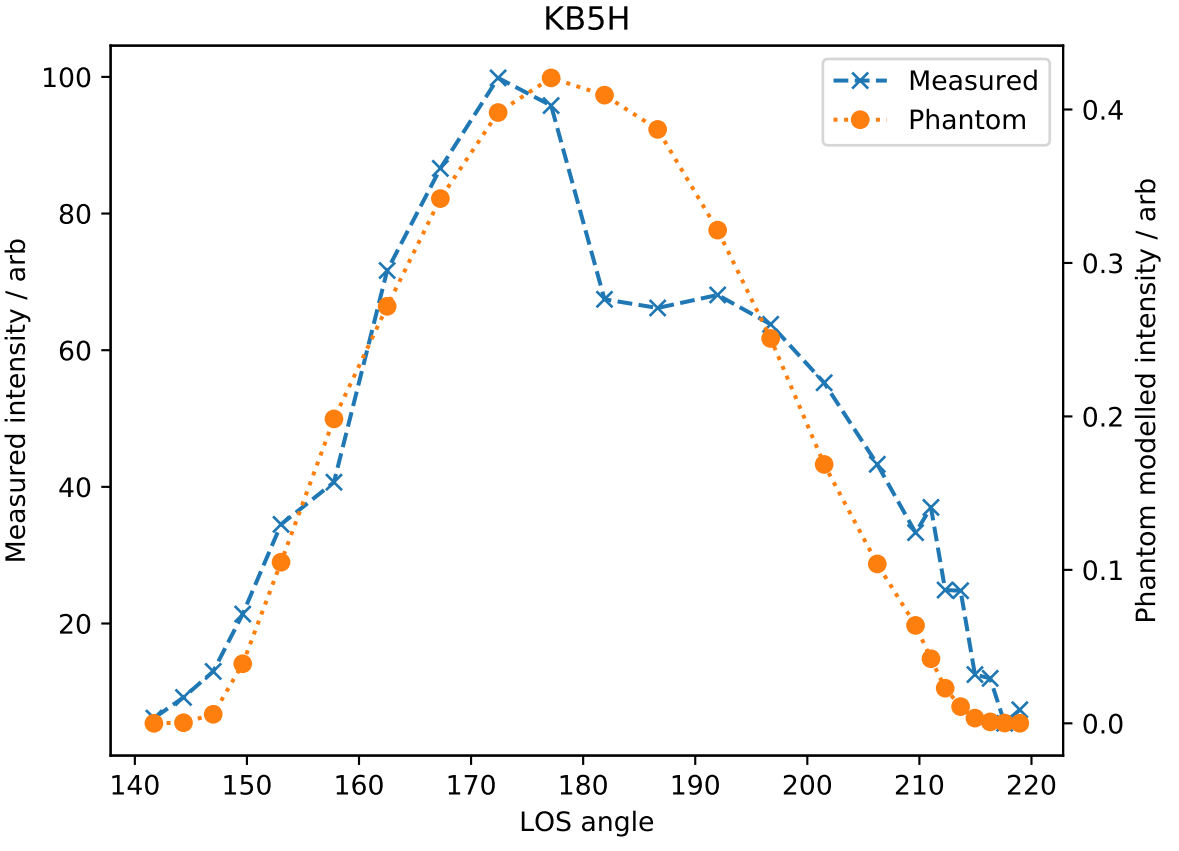
KB5H
Measured
Phantom
Measured intensity / arb
Phantom modelled intensity / arb
LOS angle
100
80
60
40
20
0.4
0.3
0.2
0.1
0.0
140
150
160
170
180
190
200
210
220

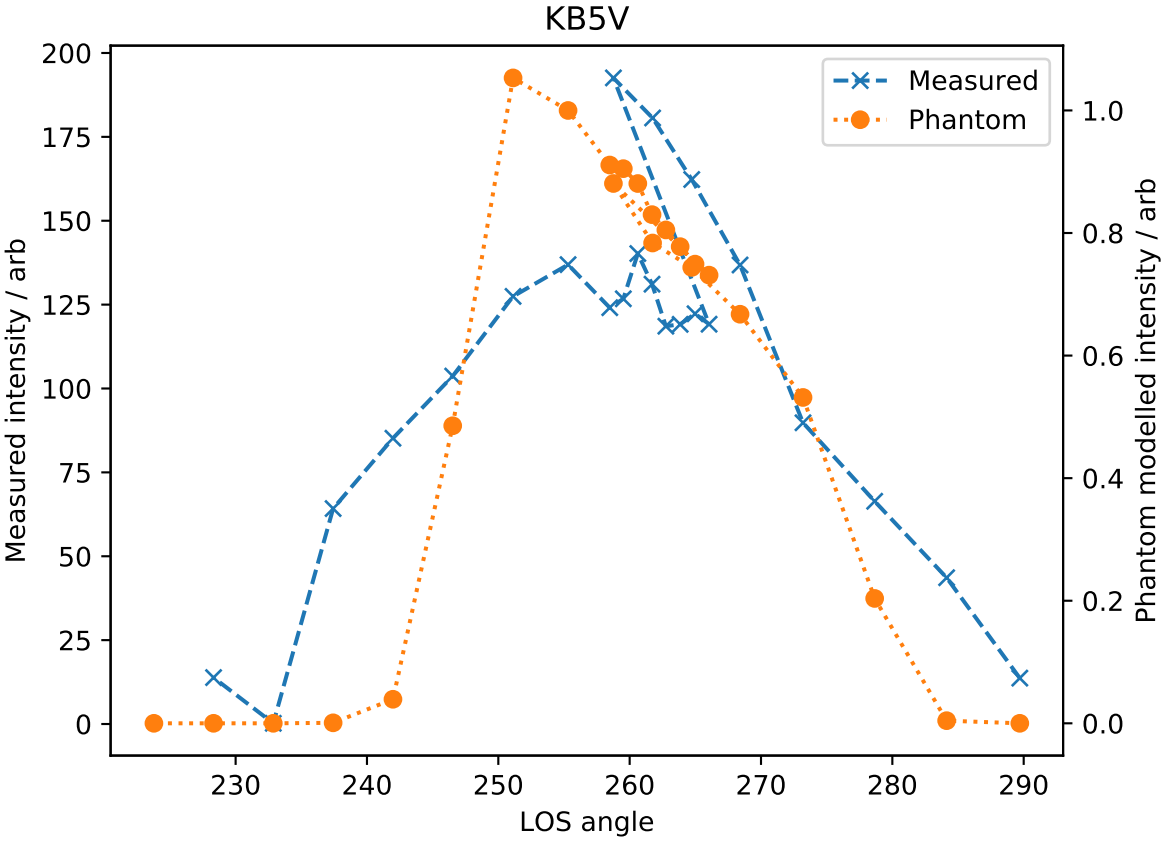
KB5V
Measured
Phantom
Measured intensity / arb
Phantom modelled intensity / arb
LOS angle
200
175
150
125
100
75
50
25
0
1.0
0.8
0.6
0.4
0.2
0.0
230
240
250
260
270
280
290

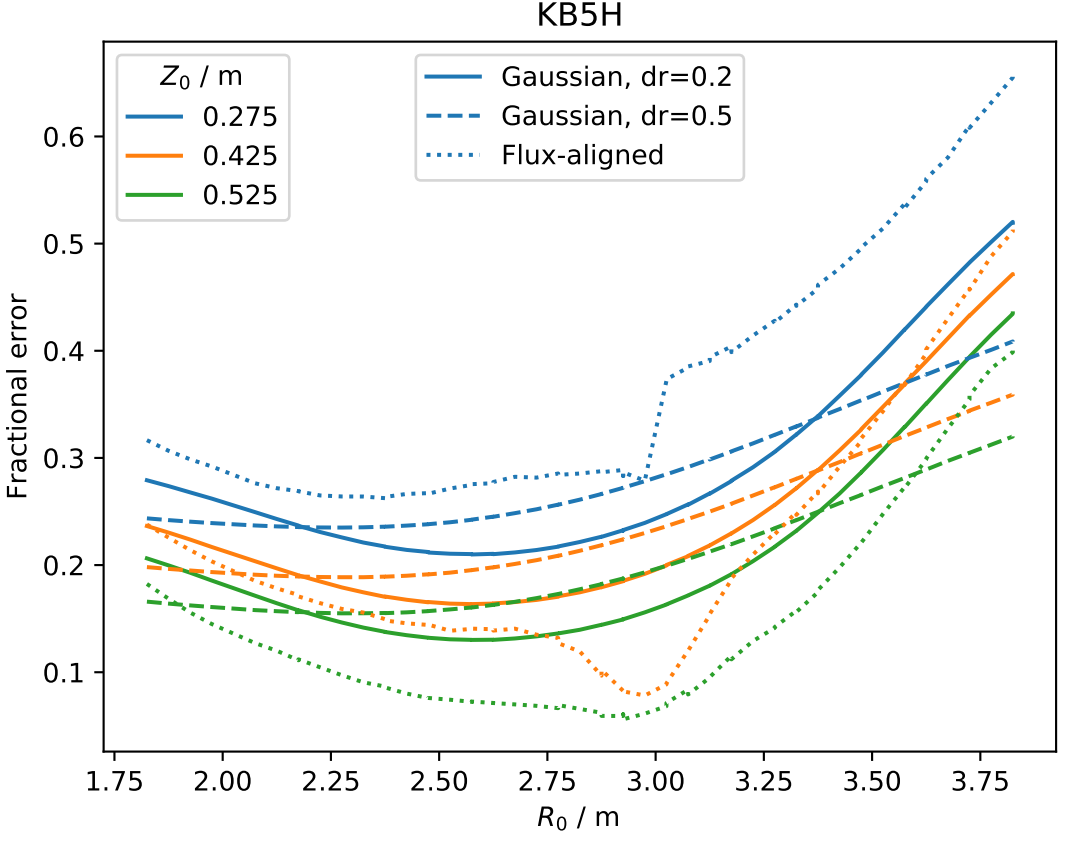
KB5H
Z_0 / m
0.275
0.425
0.525
Gaussian, dr=0.2
Gaussian, dr=0.5
Flux-aligned
Fractional error
0.1
0.2
0.3
0.4
0.5
0.6
1.75
2.00
2.25
2.50
2.75
3.00
3.25
3.50
3.75
R_0 / m

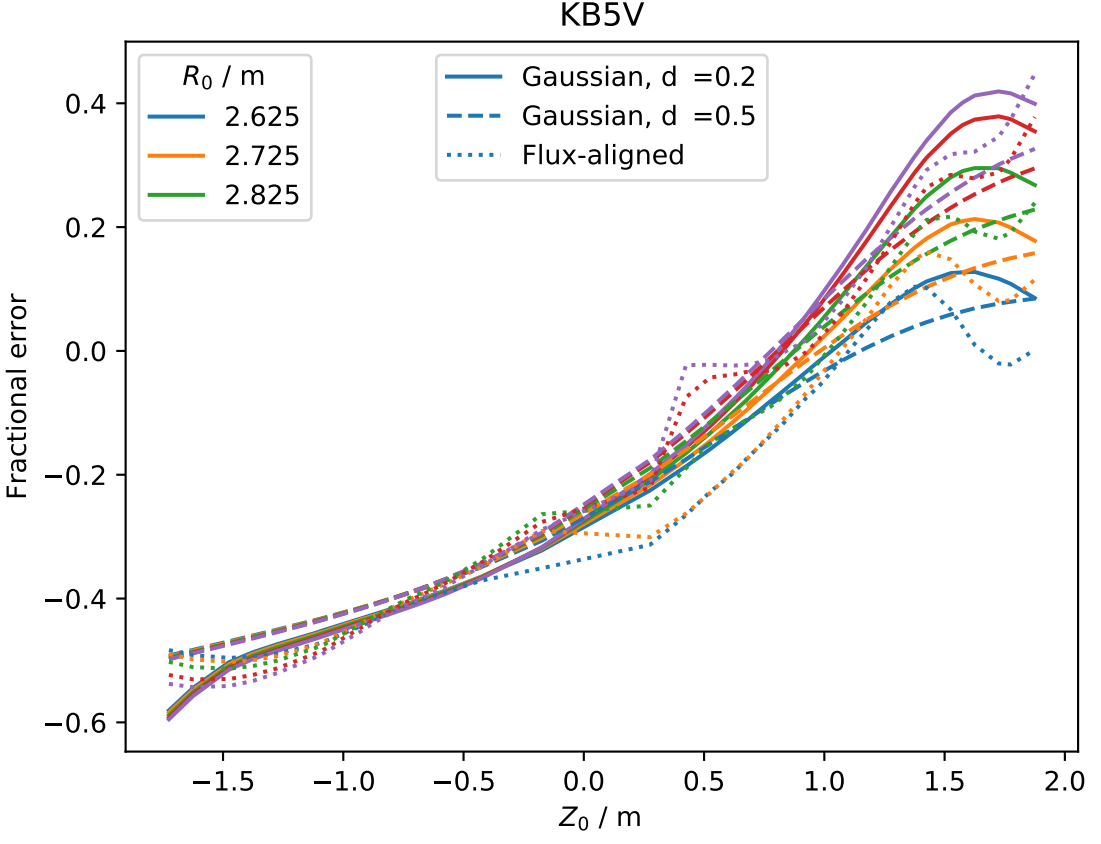
KB5V
R_0 / m
2.625
2.725
2.825
Gaussian, d =0.2
Gaussian, d =0.5
Flux-aligned
Fractional error
0.4
0.2
0.0
−0.2
−0.4
−0.6
−1.5
−1.0
−0.5
0.0
0.5
1.0
1.5
2.0
Z_0 / m